Global and Planetary Change 205 (2021) 103611

Contents lists available at ScienceDirect

Global and Planetary Change

journal homepage: www.elsevier.com/locate/gloplacha

The Congo Basin: Subsurface structure interpreted using potential field data and constrained by seismic data

Francesca Maddaloni [a], Carla Braitenberg [a], Mikhail K. Kaban [b,c], Magdala Tesauro [a,d,*], Damien Delvaux [e]

[a] University of Trieste, Department of Mathematics and Geoscience, Trieste, Italy
[b] German Research Center for Geosciences (GFZ), Potsdam, Germany
[c] Schmidt Institute of Physics of the Earth, Moscow, Russia
[d] University of Utrecht, Department of Geosciences, the Netherlands
[e] Royal Museum for Central Africa, Dept. Earth Sciences, Tervuren, Belgium

ARTICLE INFO

Editor: Zhengtang Guo

Keywords:
Congo basin
Gravity residuals
Regression analysis
Gravity effect of sediments

ABSTRACT

The Congo Basin (CB) occupies a large part of the Congo Craton, which formed from the amalgamation of different cratonic blocks of Archean age. It records the history of deposition of up to 1 Gyr of sediments, one of the longest geological records on Earth above a crystalline basement. It is considered as a typical intracratonic basin, with its slow and long-lived subsidence history and the largely unknown formation mechanisms. In this study, we analyze the gravity field in the central area of the CB, applying two different methodologies to investigate the depth of the crystalline rock basement and crustal structures. The crustal contribution to the gravity observations is determined in one case by a data driven approach, while in the other using an isostatic compensation model that includes the effect of the rigidity of the lithosphere. Both methods are constrained by density measurements from rock samples/boreholes and interpretations of the reflection seismic profiles, crossing the CB. The results obtained are quite consistent with the aeromagnetic anomalies, showing structural highs and lows, NW-SE trending, matching the axial magnetic zone. The maximum basement depth is between 10 and 18 km, depending on the gravity method and assumptions used. Furthermore, we could identify several small basins that from the interpolation of seismic profiles are not clearly resolved, such as Busira (7–9 km deep), Lokoro (10.5–12 km deep), and Salonga basins (10–11.5 km deep), in the northwestern, southeastern, and central sector of the CB, respectively. The analysis of the gravity anomalies mainly related to the crystalline crust supposes the presence of high-density bodies located in the southern part of the CB that we interpreted as related to the extensional phases that initiated the subsidence of the basin.

1. Introduction

The Congo Basin (CB), with its bowl-shape straddles the equator in central Africa and occupies a large part of the Congo Craton (~1.2 million km^2, Fig. 1). Geological and geophysical investigations in the CB started in the 1950's with field works, gravity, and seismic surveys. During geophysical surveys, organized by a consortium of oil companies in the 1970's, about 2600 km of seismic reflection profiles have been shot in the central part of the CB (Fig. 1). Furthermore, in order to reconstruct the tectonic evolution of the CB, four stratigraphic wells were drilled, the first two by REMINA (Société de Recherche Minière en Afrique), in the localities of Samba (2.039 m deep; Cahen et al., 1959) and Dekese (1.856 m deep; Cahen et al., 1960). The other two were drilled in 1981 by Esso Zaire (1981a,b) (Mbandaka-1 and Gilson-1, 4300 m and 4700 m deep, respectively). Unfortunately, none of the four wells located inside the CB reached the basement (Delvaux et al., 2021).

The availability of a high-resolution global gravity field dataset derived from the GOCE (Gravity field and steady-state Ocean Circulation Explorer) satellite gives the opportunity to recover geological features across the entire African continent, also in areas with scarce terrestrial field observations (Braitenberg, 2015). Satellite gravity data revealed a huge free-air and geoid anomaly centered on the CB (Braitenberg and Ebbing, 2009) that previous studies linked to the mantle structure and

---

* Corresponding author at: University of Trieste, Department of Mathematics and Geoscience, Trieste, Italy.
E-mail address: mtesauro@units.it (M. Tesauro).

https://doi.org/10.1016/j.gloplacha.2021.103611
Received 3 March 2021; Received in revised form 15 July 2021; Accepted 3 August 2021

its dynamics (Downey and Gurnis, 2009; Crosby et al., 2010) or to the effect of sediments (Buiter et al., 2012). However, without knowing the basin structure in detail, it is hard to validate them. Residual gravity maps displayed in Kadima (2011) and Kadima et al. (2015) show a very well defined linear positive trend with a NW-SE direction, coinciding with the Pan-African deformation area observed on seismic lines (Daly et al., 1992; Lawrence and Makazu, 1988).

Gravity data, together with other geological and geophysical data, were used by Watts et al. (2018) to compare the structure, subsidence history, and evolution of several intracratonic basins including the CB. In this study, it was proposed that the observed gravity anomalies in the CB might be partly explained by high-density igneous rocks, which contributed to the basin subsidence and consequent sediment accumulation. Kaban et al. (2021) reconstructed the basement depth of the CB, based on the inversion of the decompensative gravity anomalies, a method developed in Kaban et al. (2017), and using as input the values of density and depths of the main sedimentary layers of Kadima et al. (2011a). In the recent study of Delvaux et al. (2021), all available geological and seismic data (reflection and refraction seismic, borehole, and field data) were used to reconstruct the stratigraphy and tectonic evolution of the CB. The seismic reflection profiles were interpreted and interpolated in order to obtain the depth of the basement (seismic basement) and isobath maps of eight horizons, corresponding to the main seismic reflectors and isopach maps of the sedimentary sequences overlying the basement. These maps revealed the existence of local and regional sedimentary deposits of various sizes that originated from several rift phases and increased their depth during the compressional tectonics that accompanied the Gondwana assembly. These basins belong to two large depressions that are separated by the Kiri High, which appeared during the initial stage of the CB (Fig. 2). However, the seismic data do not have a uniform distribution and their interpolation could have produced artefacts in the uncovered regions. In particular, specific features observed in correspondence of the seismic lines are extruded laterally. Examples are the NE-extension of the Lomami basin and the SE-extension of the Lokonia High (Fig. 2).

In this study, we use all available aeromagnetic and gravity data to delineate the main structures of the basement and overlying sediments. In this way, we can obtain information on basement depth in the areas between the seismic lines, which can only be retrieved otherwise by interpolation. Furthermore, we can extend the model laterally to the areas of the CB uncovered by the seismic data, where the crystalline basement is still poorly explored by other geophysical surveys. We reconstruct the depth of the basement, applying two different gravity methods, reducing inherent ambiguities specific to each method, and verifying the agreement between the modelled and observed gravity field. The use of two different methods gives us the chance to check the reliability of the final solution.

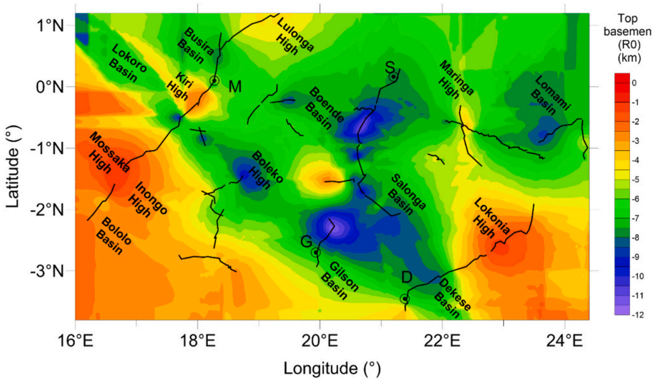

Fig. 2. Main tectonic structures identified at the top of the seismic rock basement (depth to the basement based on the interpretation and interpolation of seismic profiles). Broken black lines show location of the seismic reflection profiles. Black circles show location of four wells drilled in the study area: D = Dekese; G = Gilson-1; M = Mbandaka-1; S = Samba (modified after Delvaux et al., 2021).

In Fig. 3, we display the main steps of the two gravity methods applied in this study. In the first method, we used the isopach maps of the sedimentary sequences (Delvaux et al., 2021) and their densities obtained from core/outcrop samples, stored at the Royal Museum of Central Africa (RMCA, Belgium), to calculate the gravity effect of sediments (*G_SED*). The residuals of the regression analysis between the

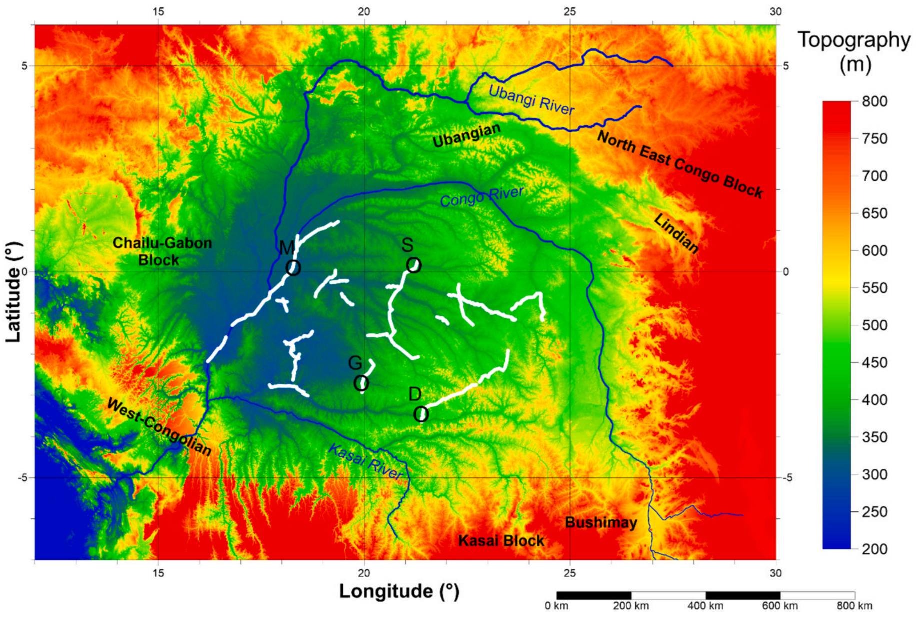

Fig. 1. Topography map of the CB using ETOPO 1 (Amante and Eakins, 2009). White lines show location of the seismic reflection profiles. The hydrological system is displayed in blue. Black circles show location of four wells drilled in the study area: D = Dekese; G = Gilson-1; M = Mbandaka-1; S = Samba (modified after Delvaux et al., 2021). (For interpretation of the references to colour in this figure legend, the reader is referred to the web version of this article.)

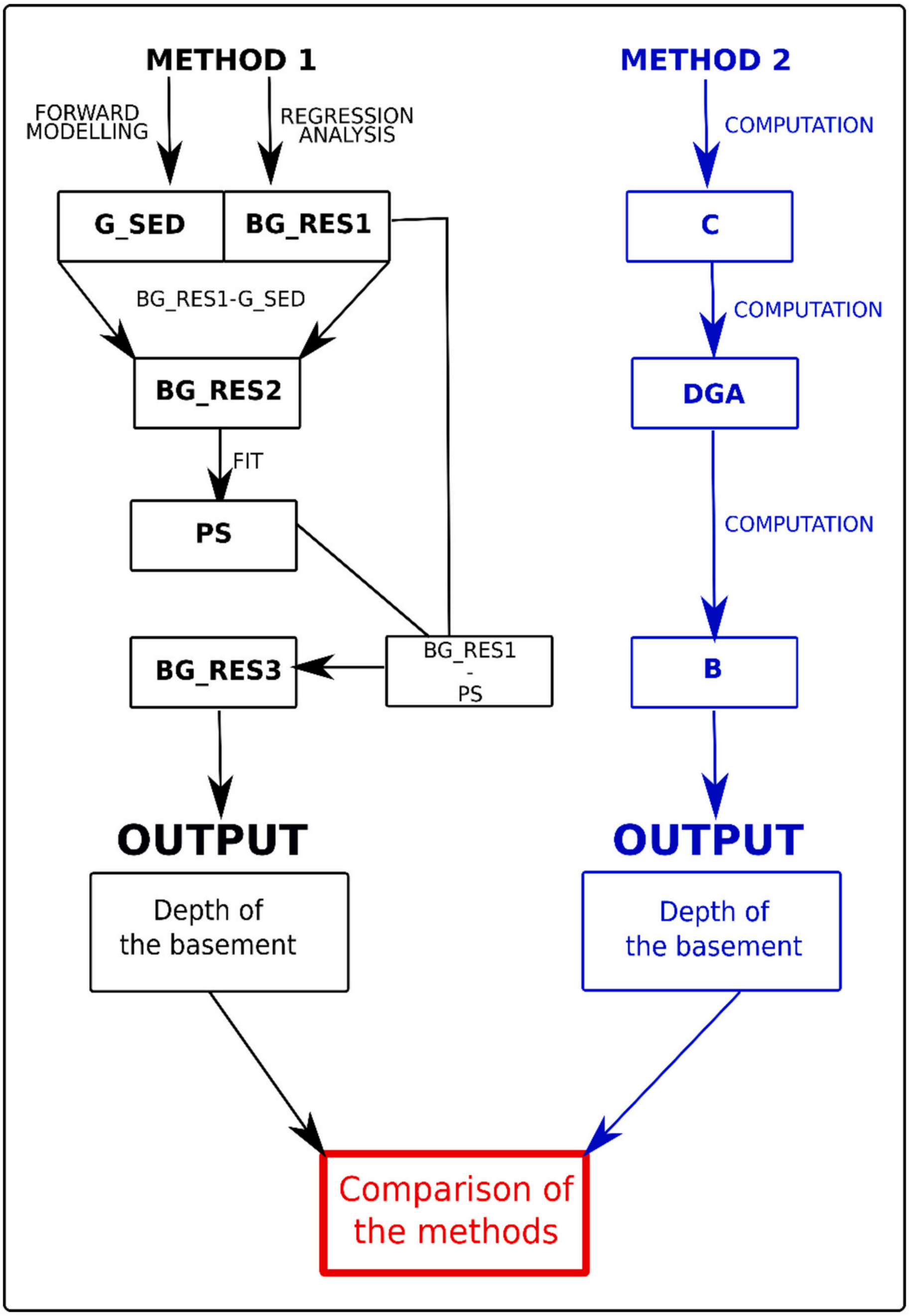

Fig. 3. Flowchart illustrating the two main investigation methods used. Abbreviations are as follows: G_SED: gravity effect of sediments. BG_RES1: residuals from regression analysis. BG_RES2: residuals obtained subtracting G_SED from BG_RES1. PS: Polynomial Surface. BG_RES3: residuals obtained subtracting PS from BG_RES1. C: amount of isostatic compensation. DGA: Decompensative gravity anomaly field. B: coefficient that controls the increase rate of the density with depth.

Bouguer anomalies and topography (*BG_RES1*) reflect the gravity effect cleared from the crustal thickness variations. The sub-crustal contributions to the gravity field are estimated by fitting a low order polynomial surface (*PS*) to the gravity field corrected for the interpolated sediments (*BG_RES2* = *BG_RES1* - *G_SED*) and for the crustal thickness variations (*BG_RES3* = *BG_RES1*- *PS*). Then, we inverted *BG_RES3* for the depth of the basement, using the seismic data as constraints and two different superficial density contrasts between sediments and the crystalline basement, to test the reliability of the results. The depth of the basement is further obtained through the inversion of the decompensative gravity anomalies with an exponential sedimentary density-depth relationship constrained by the available seismic data. In the first step, we calculated the isostatic gravity anomalies (*C* in Fig. 3). In this way, it was possible to remove the effect of deep density heterogeneities when only a little is known about actual structure of the lower crust, Moho, and upper mantle (Blakely, 1995). However, the effect of sediments was largely reduced in the isostatic gravity field, since density anomalies of the sedimentary cover were also compensated. In case of the CB, the gravity field of sediments might be reduced by one order of magnitude or even more (Kaban et al., 2021). To recover this effect, we applied the decompensative correction (Zorin et al., 1985; Cordell et al., 1991), which was further improved to account, for the effect of elastic deformations of the lithosphere (Kaban et al., 2017, 2021). In the next step, the decompensative gravity anomalies (DGA) were compared with existing seismic determinations to define the density-depth relations, which fit in the best way the calculated anomalies and seismically determined depths to the basement. Finally, these relationships are employed to calculate the basement depths, based on the decompensative gravity anomalies for the whole basin, using a constant and variable *B* (*B*, in Fig. 3), a coefficient, which controls the increase rate of the density with depth. Finally, we discussed the results and compared them with the depth of the seismic basement (Fig. 2).

2. Tectonic setting

The CB started to form in the late Mesoproterozoic, over the Precambrian basement of Central Africa (Fig. 4), likely from a rift phase (Delvaux et al., 2021). The basement is part of the Congo Craton (Cahen, 1983a, 1983b), which is composed of an assemblage of Archean nuclei (including the Tanzanian craton), welded together by Meso-and Paleoproterozoic belts (de Waele et al., 2008; de Wit and Linol, 2015). It is surrounded from all sides by Neoproterozoic belts (Abdelsalaam et al., 2002; Frimmel et al., 2006; Gray et al., 2008; Collins and Pisarevsky, 2005; Fritz et al., 2013; Foster et al., 2015). As shown in Delvaux et al. (2021), the initial rift and post-rift phases of the Meso- and Neoproterozoic age produced significant subsidence of the basement in the northern part of the CB. The compressional tectonics, associated to the assembly of the Gondwana supercontinent, between 550 and 530 Ma, is expressed by both folding and faults of the Proterozoic sediments and underlying basement. This event caused further subsidence and localized uplifts. Post-orogenic extension and denudation occurred in the early Paleozoic, with consequent development of an unconformity and post-orogenic sedimentation in the Cambrian to the Devonian. The sedimentation was interrupted by the Gondwana glaciation occurred during the Late Devonian – Early Carboniferous, when the CB was located on the South Pole. Since then, the CB drifted northwards to reach the present-day equatorial position. The CB was tectonically reactivated at the end of the Permian to early Triassic, in response to the far-field effect of the Gondwanides orogeny along the southern margin of Gondwana. Diachronous Gondwana break-up and drifting started at 200 Ma. It was followed by continental to lacustrine sedimentation during late Jurassic to Cretaceous age. During the Paleogene, significant

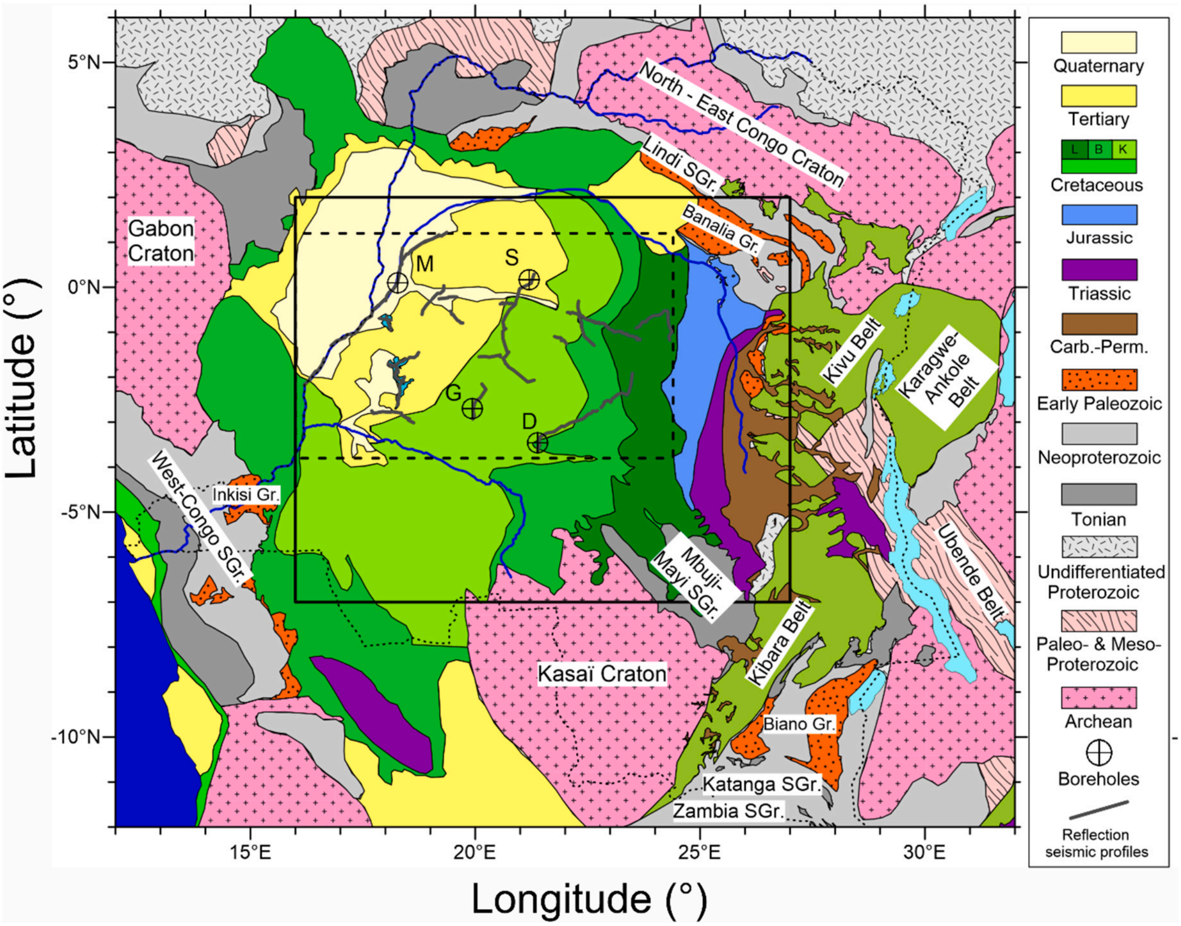

Fig. 4. - Surface geology of the CB (modified after Kadima et al., 2015). Broken gray lines show location of the seismic reflection profiles. Black circles: deep wells: D (Dekese), G (Gilson-1), M (Mbandaka-1). The continuous black rectangle delimits the area displayed in Fig. 5, while the dashed black rectangle delimits the central area of the CB as the study area (modified after Delvaux et al., 2021).

denudation occurred, removing up to 1000 m of sediments. General uplift of the southern half of the African Continent and East African rifting, together with ridge push forces from the Central Atlantic, produced uplift and erosion in the external parts of the basin, giving its cuvette shape, as well as producing seismic activity (thrust and strike-slip faults), long-wavelength folding, and river incision.

3. Aeromagnetic constraints on the structure of the Congo Basin

The aeromagnetic data set is composed of two surveys. The first has been flown in 1984 by the Japan National Oil Corporation (JNOC, 1984), with a line spacing of 18,000 m, a cruising altitude of 750 m, and line direction of 0° respect to north. The two other surveys have been made in 1987 and 1986 by the Companies Générale de Géophysique (CGG), with line spacing of 9000 m, a cruising altitude of respectively 915 m and 1332 m, and a line direction of 0° respect to north. The data covers large parts of the CB in the Democratic Republic of Congo (DRC) and an adjacent part in the Congo Republic. The release of magnetic data from GETECH (Geoscience data and geospatial technology for delivering the energy transition) group (Leeds, UK) has been done in the frame of a scientific collaboration between the RMCA and GETECH.

The total field magnetic data have been extracted from the GETECH 1 km x1 km grid, compiled by the African Magnetic Mapping Project (AMMP) at Leeds University. The compilation is in the form of a unified grid of 1 km x1 km of total magnetic intensities (TMI). The original data have been merged, projected in an equatorial Mercator projection and interpolated on a regular grid of 1 km × 1 km (Barritt, 1983). Afterwards, the data have been reduced to the North Pole, in order to display the magnetic anomalies over the inducing bodies. The magnetic bodies are identified by positive anomalies and the magnetic lineaments correspond to sharp lateral change in the magnetic field. The resulting map (Fig. 5) shows a prominent highly magnetic zone NW-SE oriented, in the central part of the basin, indicated as 'axial magnetic zone'. It is interpreted as the signature of a failed rift, which is supposed to have initiated the CB (Daly et al., 1992; Kadima et al., 2011b). This zone currently corresponds to the Kiri High, a prominent structure that divides the CB into a NE (Busira, Boende, and Lomami basins) and a SW part (Lokoro, Gilson, and Dekese Basin). To the NW, the extension of the Kiri High into the Republic of the Congo on the NW side of the Congo River has been also observed in the aeromagnetic data (not available to us, but displayed in Master, 2010). The SE extension of this axial magnetic zone reaches the area where the interpretation of the seismic profiles and gravity data (see below) suggests the presence of a deep basin (Salonga Basin). The positive anomaly in the NE corresponds to the Lindi Supergroup, covered by relatively thin sediments (Kadima et al., 2015), and the positive anomaly around Lake Mai-Ndombe corresponds to the Inongo High (Fig. 5). In the extreme west, the positive anomaly marks the western limit of the CB. Towards the south, closely spaced and very short wavelength anomalies mark the signature of the highly magnetic Kasaï cratonic block under a thin sedimentary cover (e.g. Roberts et al., 2015). These anomalies do not show the typical signature of the deep Lokoro – Gilson – Dekese basins and trace the approximate southern limit of the CB. They are flanked by an alignment of strong negative anomalies that extend SE of the Dekese well site,

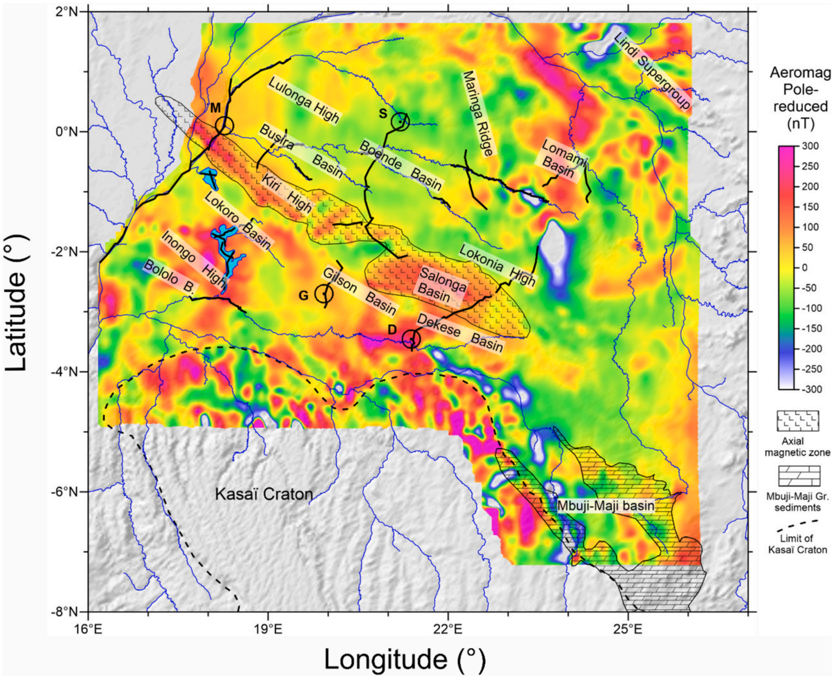

Fig. 5. - Aeromagnetic map reduced to the North Pole overlain by the axial magnetic zone. Thick dashed line shows the approximate northern limits of the Kasaï Craton interpreted from aeromagnetic data. Broken black lines show location of the seismic reflection profiles. Black circles show location of four wells drilled in the study area: D = Dekese; G = Gilson-1; M = Mbandaka-1; S = Samba.

Table 1

Age and average density of the major stratigraphic horizons used for the calculation of density contrast, existing between each layer and the reference crustal density (2.67 g/cm^3).

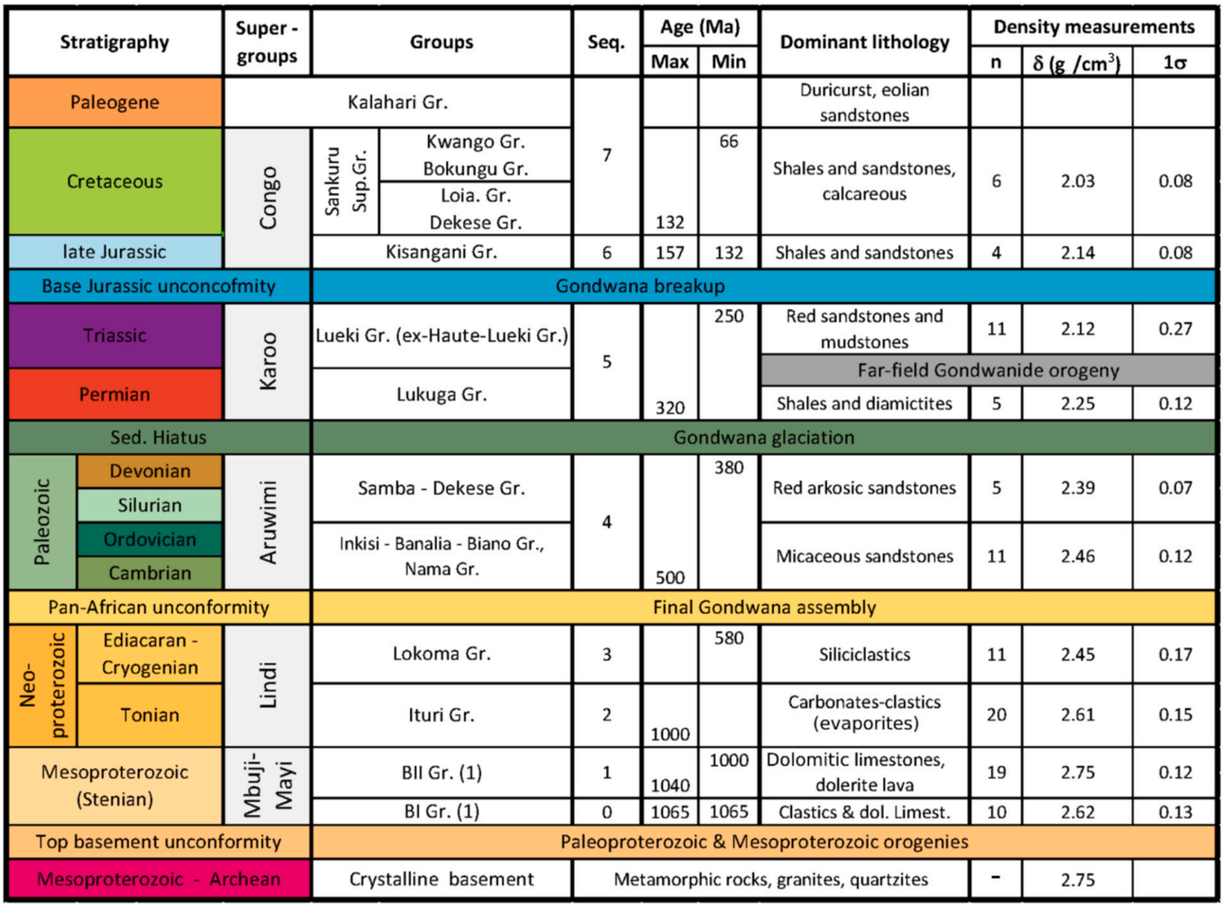

Stratigraphy		Super - groups	Groups		Seq.	Age (Ma)		Dominant lithology	Density measurements		
						Max	Min		n	δ (g /cm^3)	1σ
Paleogene			Kalahari Gr.		7			Duricurst, eolian sandstones			
Cretaceous		Congo	Sankuru Sup.Gr.	Kwango Gr. Bokungu Gr.		132	66	Shales and sandstones, calcareous	6	2.03	0.08
				Loia. Gr. Dekese Gr.							
late Jurassic			Kisangani Gr.		6	157	132	Shales and sandstones	4	2.14	0.08
Base Jurassic unconcofmity			Gondwana breakup								
Triassic		Karoo	Lueki Gr. (ex-Haute-Lueki Gr.)		5	320	250	Red sandstones and mudstones	11	2.12	0.27
								Far-field Gondwanide orogeny			
Permian			Lukuga Gr.					Shales and diamictites	5	2.25	0.12
Sed. Hiatus			Gondwana glaciation								
Paleozoic	Devonian	Aruwimi	Samba - Dekese Gr.		4	500	380	Red arkosic sandstones	5	2.39	0.07
	Silurian										
	Ordovician		Inkisi - Banalia - Biano Gr., Nama Gr.					Micaceous sandstones	11	2.46	0.12
	Cambrian										
Pan-African unconformity			Final Gondwana assembly								
Neo-proterozoic	Ediacaran - Cryogenian	Lindi	Lokoma Gr.		3		580	Siliciclastics	11	2.45	0.17
	Tonian		Ituri Gr.		2	1000		Carbonates-clastics (evaporites)	20	2.61	0.15
Mesoproterozoic (Stenian)		Mbuji-Mayi	BII Gr. (1)		1	1040	1000	Dolomitic limestones, dolerite lava	19	2.75	0.12
			BI Gr. (1)		0	1065	1065	Clastics & dol. Limest.	10	2.62	0.13
Top basement unconformity			Paleoproterozoic & Mesoproterozoic orogenies								
Mesoproterozoic - Archean			Crystalline basement					Metamorphic rocks, granites, quartzites	-	2.75	

which suggests an interaction between the Kasaï craton and the Dekese Basin. We draw the limit of the Kasaï craton, taking into account the interpolation of the refraction seismic data for both the 4200 ms and 5200 ms refractors (Delvaux et al., 2021), and the outcropping field of the late Mesoproterozoic Mbuj-Maji Group (basal sequences Seq0 and Seq1 in Table 1). It shows a southward 'gulf' of the CB sediments between two lobes of the Kasaï Craton (Fig. 5). The aeromagnetic data show also a structural continuity between the CB and the Mbuji-Maji Basin towards the SE, confirming the assumption made (Delvaux et al., 2021) that the latter could represent the outcropping part of the basal series of the CB.

4. Gravity data

The gravity field is derived from the gravity model (EIGEN-6C4, Förste et al., 2014) available in spherical harmonic expansion, obtained by combining satellite observations, from the satellites GOCE, LAGEOS, GRACE and terrestrial data. The term EIGEN means European Improved Gravity model of the Earth by New techniques and EIGEN-6C4 model is the latest release (year 2014) of the EIGEN-6 -Series. The field has been published with maximum degree/order 2190, which corresponds to a spatial resolution at the equator of 9 km. It is customary to obtain the Bouguer gravity field reducing the gravity field for the effect of topography (SM-Fig. 1). We adopt a global correction of topography that is the effect of the topography, which has been estimated on the entire globe and then the effect is displayed in terms of the spherical harmonical expansion, again to maximum degree and order 2190, to match the available gravity field. Essentially two groups have worked on this subject (Rexer et al., 2016; Grombein et al., 2016) and have published two models, which are very similar to each other and for our purpose can be used choosing either one of them. We have used the REQ_TOPO_2015_plusGRS80, which takes into account the rock topography (SM-Fig. 1), water and ice-cover, according to the terrain-model Earth2014 (Hirt and Rexer, 2015), discretizing and calculating the mass effect with tesseroids (Uieda et al., 2016). The gravity effect of the topography, obtained using the REQ_TOPO_2015_plusGRS80 model, is negative and spans from −96 mGal to −50 mGal, with a general increase from west to east (SM-Fig. 1).

The gravity disturbance (Fig. 6A) spans from −105 mGal to 20 mGal. The CB is mostly characterized by negative anomalies with average values around −80 mGal. We observe a series of NW-SE oriented negative and positive anomalies, corresponding to the alternation of highs and basins. The Bouguer anomalies (Fig. 6B) have been calculated subtracting the gravity effect of the topography (REQ model, SM-Fig. 7) from the gravity disturbance. The anomalies range between −15 mGal to 115 mGal, with the minimum values forming sub-circular anomalies, which may be related to the sedimentary deposits and/or low-density bodies in the shallow crust. The maximum values are located in correspondence of the Kiri High and in the southern part of the CB.

5. Gravity effect of the sedimentary thickness

In order to compute the gravity effect of sediments G_SED based on the active seismic, we discretized each sedimentary layer obtained from

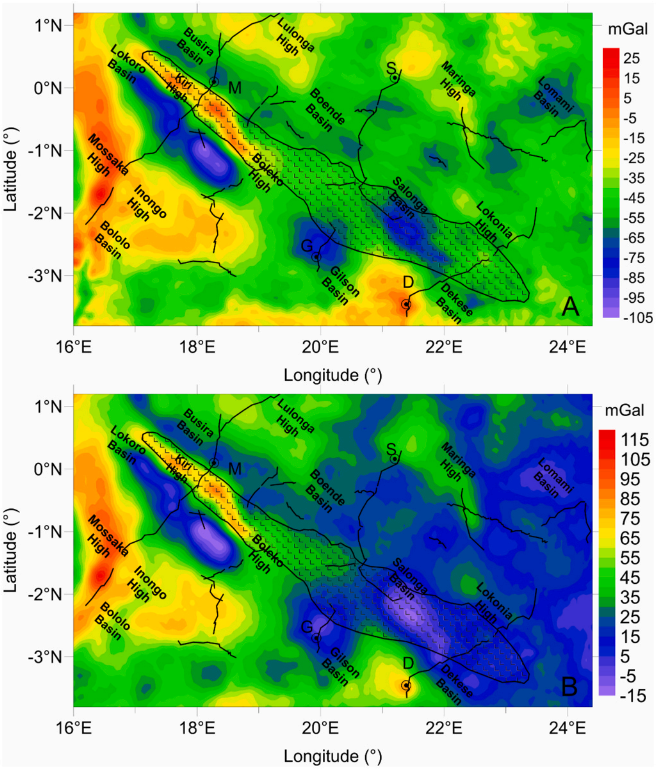

Fig. 6. Gravity disturbance (A) and Bouguer gravity anomaly (B) maps obtained from EIGEN-6C4 model, overlain by the axial magnetic zone. Broken black lines show location of the seismic reflection profiles. Black Circles display location of four wells (D = Dekese; G = Gilson-1; M = Mbandaka-1; S = Samba).

the interpolation of the seismic horizons defined by the interpretation of the seismic lines (Delvaux et al., 2021) into a grid of spherical tesseroids and calculated G_SED, with the "Tesseroids" software (Uieda et al., 2016). The density contrast of each tesseroid was computed as the difference between the densities of each sedimentary layer displayed in Table 2 and a standard reference density of crystalline basement equal to 2.67 g/cm^3.

The density of the Proterozoic sedimentary layers Seq0-Seq2 is close to that of the reference density of the crystalline basement and in particular, the density of layer Seq1 (Dolomitic limestone and dolerite lava) is even higher (Tables 1 and 2). Therefore, they give a small contribution to *G_SED*. In contrast, the layers Seq3-Seq5 show a progressively lower density upward and thus produce more pronounced density contrast with the crystalline basement. Therefore, the greatest negative values of *G_SED* (−115 mGal) correspond to the location of the deepest basins (Lokoro, Gilson, Boende and Busira Basin), characterized by the greatest thickness of the low-density sequences S3-S7 (Delvaux et al., 2021). On the other hand, the Lomami Basin, containing a greatest thickness of the high-density layers (Seq0-Seq2), shows *G_SED* values around −75 mGal (Fig. 7).

However, we should take into account that the *G_SED* field is reliable only along the seismic lines, whereas it is based on an interpolated basement depth between the lines, which we intend to verify through an inversion of the gravity field. This gravity field useful for the inversion of the basement must be cleared from the effects of crustal thickness and the sub-crustal contributions to the gravity field. We estimate the contribution of crustal thickness through a proxy method, which analyses the regression between the Bouguer field and topography and has been tested and demonstrated in several contexts (Pivetta and Braitenberg, 2020; Maddaloni et al., 2021).

6. Regression analysis between topography and Bouguer gravity anomaly field

The regression analysis between the topography and Bouguer anomalies is a statistical method that allows reducing the gravity values

Table 2
Maximum thickness of the major stratigraphic sequences (Delvaux et al., 2021) with to their average density values.

Stratigraphic sequences (N.)	Maximum thickness (km)	Density (g/cm^3)
Seq0	5.52	2.620
Seq1	1.59	2.750
Seq2	6.79	2.610
Seq3	2.99	2.480
Seq4	2.87	2.425
Seq5	1.82	2.270
Seq6	1.78	2.030

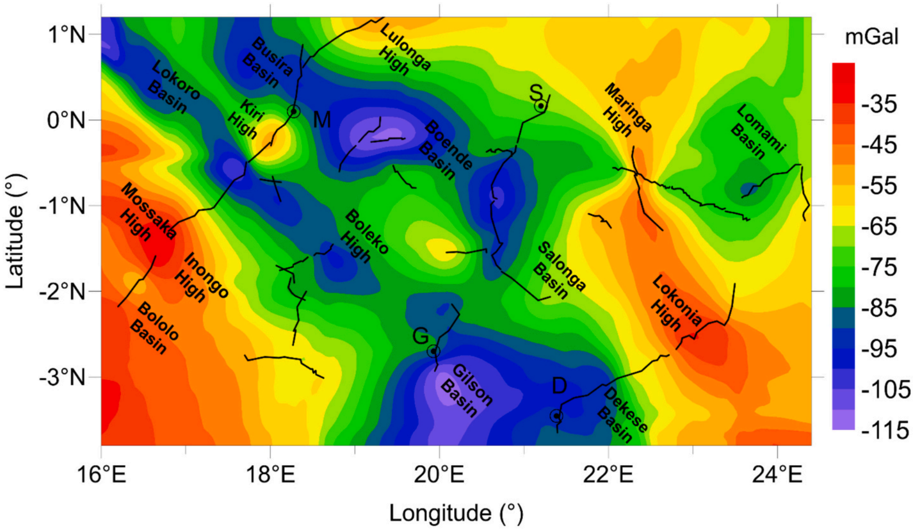

Fig. 7. Gravity effect of sediments (G_SED) in the CB based on the interpolation of seismic lines. Broken black lines show location of the seismic reflection profiles. Black circles show location of four wells drilled in the study area: D = Dekese; G = Gilson-1; M = Mbandaka-1; S = Samba.

from the effect of deep crustal layers, when a regional crustal model, based on seismic data, providing both Moho depth and velocity variations, is missing (Braitenberg, 2015; Pivetta and Braitenberg, 2020; Maddaloni et al., 2021). Since this is the case of the CB, we applied the regression analysis method, which is based on the general observation that topography is anti-correlated with the Bouguer gravity field on a global scale (as a consequence of the isostatic theory). For the lithospheric flexure model, at increasing topography wavelengths and decreasing equivalent elastic thickness, the flexural response tends towards the Airy local isostatic compensation mechanism (e.g., Watts, 2001). According to the Airy hypothesis and in the approximation of the Bouguer plate, the expected relation between Bouguer field and topography is linear:

$$BG \approx -2\pi G\,(r-d)\,(\rho_m-\rho_c) = -2\pi G\rho_c h \tag{1}$$

where $(r-d)\,(\rho_m-\rho_c)$ is the gravimetric effect of the Airy isostatic root approximated to an infinite plate analogue to the Bouguer plate; BG is the Bouguer anomaly; G is the gravitational constant (6.67430 10^{-11} $\mathrm{Nm^2/kg^2}$); d is the reference crustal thickness; r is the isostatic crustal thickness; ρ_m is the upper mantle density; h is the topography over the sea level.

The regression line carries important information on the stress state of the lithosphere, since a negative slope demonstrates the existence of an isostatic compensation mechanism. The absolute value of the slope mainly depends on the density contrast between crust and mantle, although it is also influenced by the general isostatic state of the area (if the area is completely uncompensated, the regression slope between Bouguer anomaly field and topography should be zero). The regression analysis is usually made over extended areas and the resulting residual values could be considered as a type of isostatic residuals. The mathematical expression of residuals is given by:

$$BG\_REG\,(x,y) = m^{*}topo\,(x,y) + q \tag{2}$$

$$BG\_RES1\,(x.y) = BG\_obs\,(x,y) – BG\_REG(x,y) \tag{3}$$

where *BG_obs* is the observed gravity Bouguer anomaly, *m* the angular coefficient of the regression line, topo (*x*, *y*) the low pass filtered topography, *q* the intercept, and *BG_REG* the expected Bouguer from the regression relation.

The residuals (*BG_RES1*, Fig. 8) show the gravity signal induced by the crustal density variation, after the removal of the effect of topography and isostatic crustal thickening. With respect to the isostatic flexure analysis, the regression analysis has the advantage to be independent on any isostatic parameters. The method has been tested with different synthetic models in Pivetta and Braitenberg (2020) and successfully applied in areas characterized by both high and low topography, such as the Alps, South Atlantic, and parts of Africa and South America (Braitenberg, 2015; Pivetta and Braitenberg, 2020). In our case, the regression analysis between topography and gravity is used to determine the anomalies due to the upper crustal mass inhomogeneity, reducing the Bouguer anomaly for the effect of crustal thickness variations.

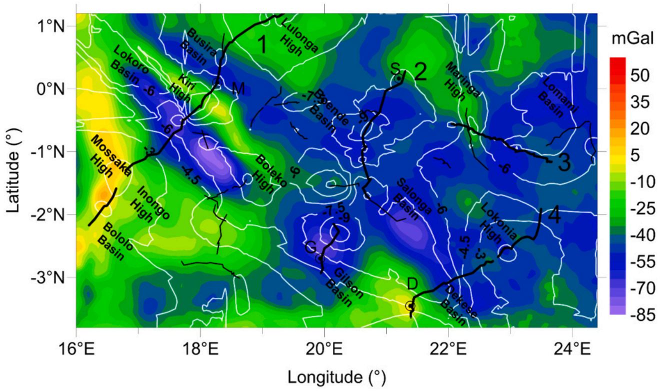

Fig. 8. Gravity residuals derived from the regression analysis between topography and Bouguer gravity anomaly field (BG_RES1). Thin broken black lines show location of the seismic reflection profiles. Thick broken black lines labelled by black numbers (placed at the end of each lines) are the chosen profiles used for the gravity analysis. White curves show the crystalline rock basement depth, reconstructed from the interpolation of the seismic reflection profiles. Black circles show location of four wells drilled in the study area: D = Dekese; G = Gilson-1; M = Mbandaka-1; S = Samba.

We performed the regression calculations for the entire CB, but we displayed the residual gravity field only for the central area of the CB (Fig. 8). It appears to have essentially negative residual gravity anomaly values, with a range from −90 mGal up to +55 mGal. We compare the gravity field with the basement depth obtained from the interpolated seismic deepest horizon, with the aim to verify the agreement between the two quantities. Qualitatively, it can be expected that gravity highs and basement highs are located in the same place and that gravity lows locate above the deepest depocenters. We observe that the basement highs are characterized by gravity residuals limited to the range of ±20 mGal, while the other areas of the CB show values that are more negative. The NW-SE trending structures, such as the Lokoro Basin, Kiri High, and Busira Basin, identified in the gravity disturbance map, is well visible by the alternation of negative and positive anomalies. The greatest positive anomaly (+40 − +50 mGal) forms a curved basement high that limits the CB on its western side (the Mossaka High). The greatest negative anomaly (−90 mGal) is located in correspondence of the Lokoro Basin. However, the anomaly's peak is shifted to NW with respect to the maximum depocenter of the basin. Other two distinct main anomalies (−70 mGal) correspond to the Gilson Basin, slightly shifted to the south with respect to the maximum interpolated sedimentary infill, and the Salonga Basin. In contrast, Lomami and Boende basins show weaker negative anomalies (−40 mGal). Therefore, there is not a strict correspondence between the basement depth and negative values of the residuals. This deviation could be due to interpolation-problems in the areas uncovered by seismic data or density variations in the sediments or shallow crystalline crust.

We plot the values of the residuals of the regression analysis against the depth of the two deepest seismic horizons (R0 and R1, Delvaux et al., 2021), along four profiles shown in Fig. 8. We can observe a good general correspondence between the lateral variations of the basement depth and residuals trend (Figs. 9–12, panels A and B). In particular, the deepest sedimentary depocenters match the most pronounced negative residuals. The direct correlation between the basement and dolomitic limestone depths with residuals is observed in the accompanying scatter plots (Figs. 9–12, panels C and D).

We define a linear model in which the coefficients have 95% of confidence bounds:

$$Line(x) = p_1{}^{*}x + p_2 \tag{4}$$

where *p1* is the slope and *p2*, the intercept of the regression lines for the rock basement and the base of the dolomitic limestones along the profiles 1, 2, 3, and 4 (Figs. 9–12, panels C and D). The values of the correlation coefficients between the residuals of the topography-Bouguer field regression analysis and depths of the crystalline basement and base of dolomitic limestones are displayed in Table 3. Profile 1 corresponds to the seismic profile R7-6-3-5-19 of Delvaux et al. (2021), Fig. 7, along the Congo River. Profile 2 corresponds to the seismic profile R60-50-51-52 of Delvaux et al. (2021) Fig. 8, across the central part of the basin, from the Gilson to the Samba well. Profile 3 corresponds to the seismic profile R15-9-10-16 of Delvaux et al. (2021) Fig. 11, across the Maringa High and the Lomami basin. Profile 4 corresponds to the seismic profile L59 of Delvaux et al. (2021) Fig. 10, calibrated by the Dekese well and L58 (not interpreted due to the poor quality).

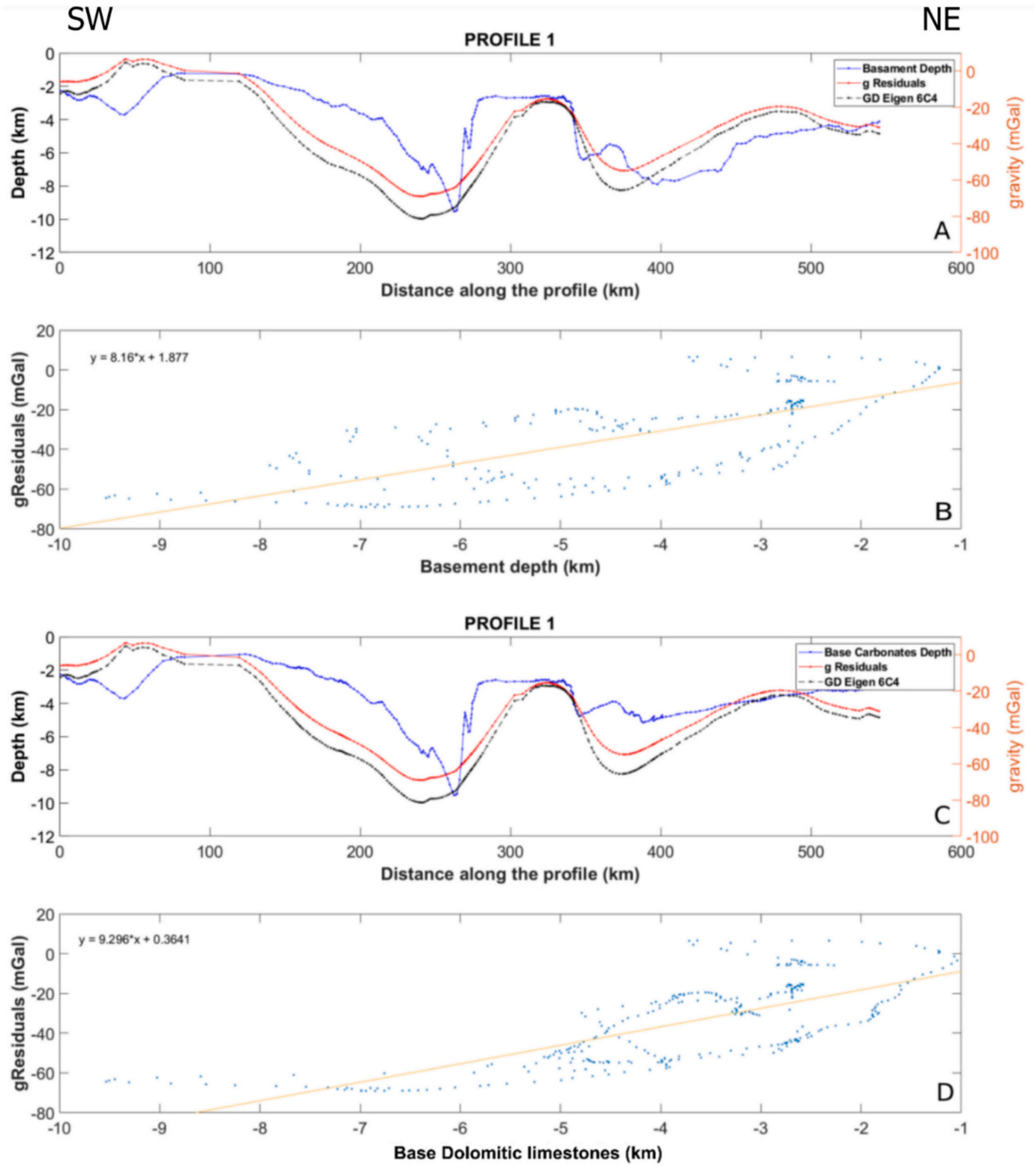

Fig. 9. Relationship between the residuals of the regression analysis, gravity disturbance, and depth of the seismic reflection horizons and scatter plot of the residuals of the regression analysis against the depth of the seismic reflection horizons along profile 1, displayed in Fig. 8.

The high correlation coefficients for profiles 1 and 3 (Table 3) demonstrate the good fit between the gravity field and the deepest horizons, with a slightly better correlation with the base of dolomitic limestones (*R1*) compared to the top basement (*R0*). This could be because the layer just above the basement contributes little to the entire mass-reduction of the sediments package. In addition, the base of the dolomitic limestone layer is better defined in the seismic profiles than the top of the basement, so the latter could be determined with less accuracy during the seismic interpretation.

The greatest values of the correlation coefficients for profile 3 could be probably due to the sedimentary sequences. The last ones have a homogeneous thickness and they are not significantly affected by the tectonic deformation (Delvaux et al., 2021). We find a much lower correlation coefficient for the profile 2, likely due to the lack of resolution in parts of the raw seismic data, a large gap in the seismic data and presence of faults. These contribute to uncertainties in the interpretation, as well as to the higher spatial resolution of the basement depth, with respect to the gravity residuals in places where sharp depth changes occur (e.g., in the faulted zones at a distance ~200–300 km). Furthermore, the residuals along profile 4 show a weak correlation with both seismic horizons (Table 3). However, we initially calculated a single linear trend as for the previous profiles, whose correlation coefficient was 0.145 and 0.165 for R1 and R0, respectively. Then, according to the two main different trends followed by the samples (Fig. 12A and C), we divided them into two groups and fitted them separately by two linear equations (Fig. 12B and D).

The steeper line (a, Fig. 12) refers to the first ~100 km along the profile: here we observed a high correlation between gravity signals and seismic basement depth. On the other hand, the less steep line (b, Fig. 12) indicates a very weak correlation between these parameters. This suggests that in this area, between Dekese Basin and Lokonia High (Profile R59, Delvaux et al., 2021), the gravity is not sensitive to the shallow basement and/or base Carbonates (R0, R1, respectively) depth variations. The systematic negative gravity anomaly is likely caused by the shallowest sedimentary sequences, which are characterized by a low density and an almost constant thickness of about 3 km all over the

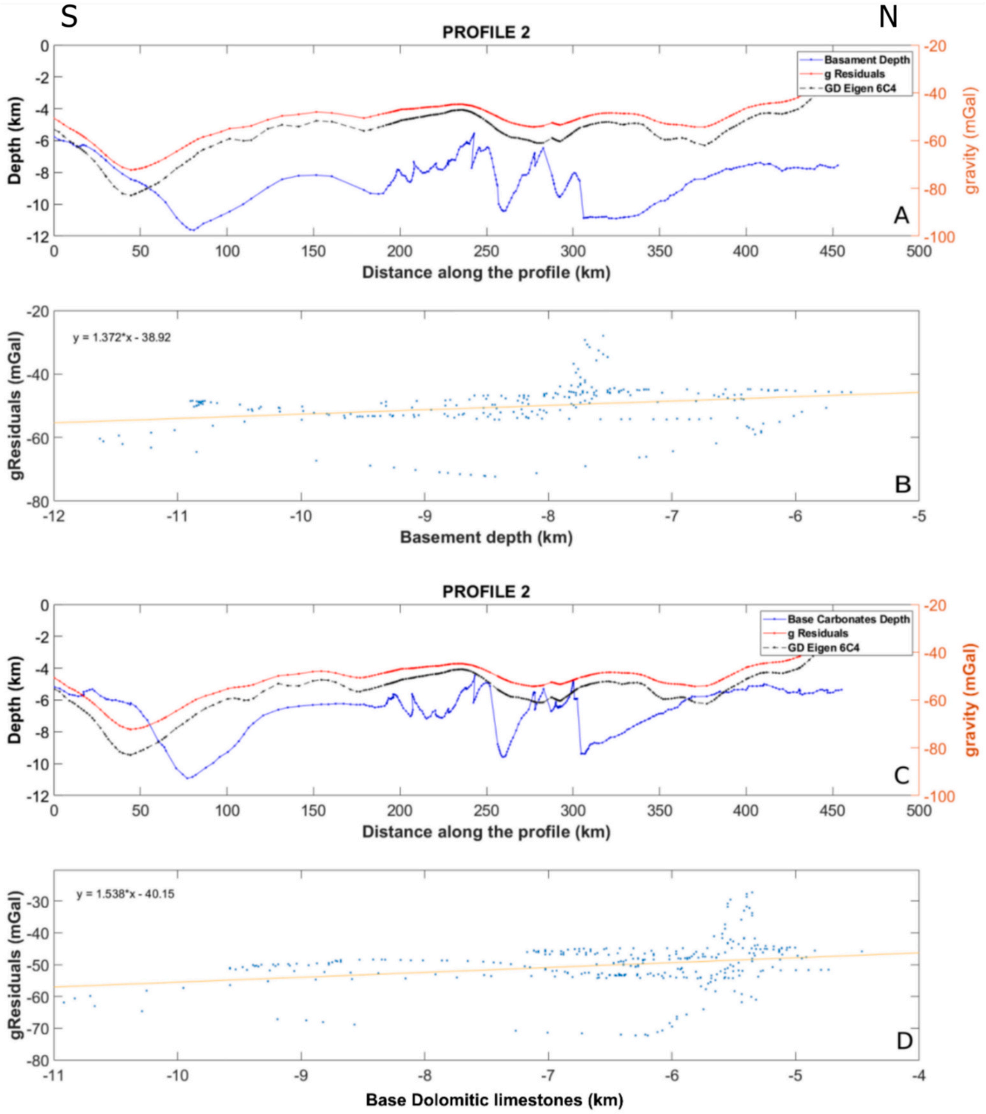

Fig. 10. Relationship between the residuals of the regression analysis, gravity disturbance, and depth of the seismic reflection horizons and scatter plot of the residuals of the regression analysis against the depth of the seismic reflection horizons along profile 2, displayed in Fig. 8.

southeastern regions (Delvaux et al., 2021).

7. Field residualization

As a first test to verify the amount of signal reduction through the gravity effect of the interpolated sediments layers, we subtracted the sedimentary gravity effect *G_SED* from the residuals of the Bouguer-Topography regression analysis (*BG_RES1*). The results are the field *BG_RES2*, in which the small-scale features due to the basement architecture variations and overlying sediments are expected to be reduced, and the average level of the residuals to oscillate around zero. If this is not the case, for instance if the field has a systematic positive upward shift, it represents the gravity effect of increased density variations at some depth level in the crustal and sub-crustal lithosphere (Fig. 13). The short wavelength part of the field can represent flaws in the basement depth and consequently in the sediment layer thickness, due to interpolation between the seismic lines. The new residuals (Fig. 13), which have reduced short wavelength signal, span between −20 and +110 mGal and are systematically positive in most of the CB. These results are in agreement with the gravity anomalies obtained by Watts et al. (2018), removing the calculated gravity effect of sediments from the Bouguer anomaly, with the assumption of a density contrast with the crystalline basement of 2.7 g/cm^3 and applying a high-pass filter to the gravity field to remove the very long wavelength contributions. In particular, the results agree in the central area of the CB, where Watts et al. (2018) show a gravity anomaly high between 40 and 60 mGal and negative anomalies along the edge of the basin. Some differences are present across the Kiri High and Lokoro Basin, where the values of *BG_RES2* (Fig. 13) span from +70 mGal to +10 mGal respectively, while the gravity anomalies of Watts et al. (2018) are weakly negative. In contrast, the Lokonia High is characterized by a well distinct positive anomaly in Watts et al. (2018), while it shows weak negative values of *BG_RES2*. The strong linear positive-negative gravity field of the Kiri High and adjacent basins is very much reduced, although larger scale positive values located in the Kiri, Boleko, and Mossaka High (between +40 and + 80 mGal) are present. They might be related to an increase of crustal density, due to the intrusion of mafic bodies (2.8–3.0 g/cm^3), which likely occurred during the rift phase that initiated the subsidence of the CB. High positive values, likely of similar origin, are also observed in the southern part of the Dekese Basin (+96 mGal). The most negative values cover the eastern part of the CB, between the Salonga and Lomami basins and in the Lokonia High (−12 mGal), suggesting the presence of a

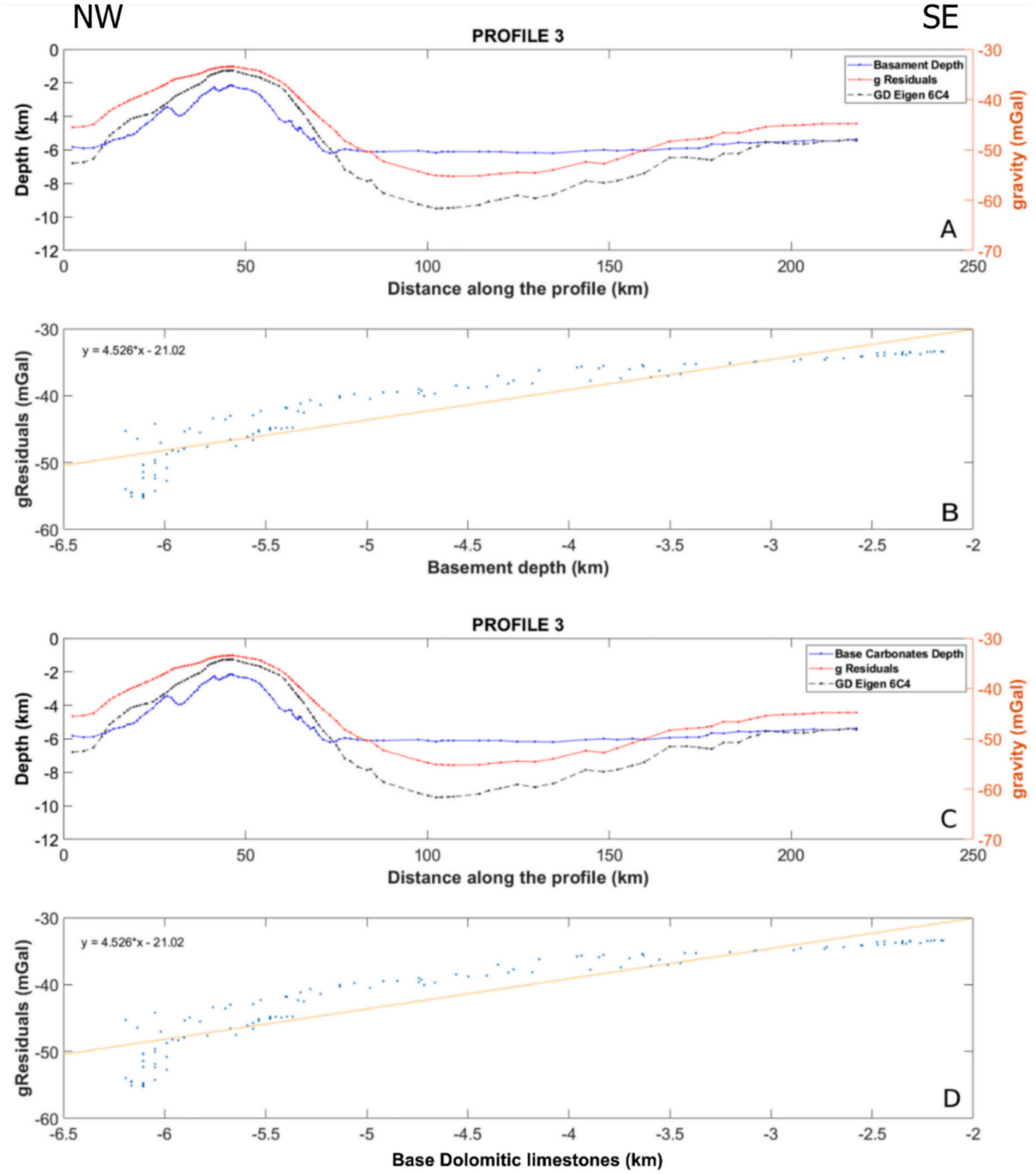

Fig. 11. Relationship between the residuals of the regression analysis, gravity disturbance and depth of the seismic reflection horizons and scatter plot of the residuals of the regression analysis against the depth of the seismic reflection horizons along profile 3, displayed in Fig. 8.

different crustal type (e.g., a more sialic crust). Other sedimentary depocenters show weak positive residuals (<+35 mGal), such as the deepest part of the Lokoro and Lomami basins. This indicates that the gravity effect of sediments obtained from the interpolated seismic lines correctly reduced small-scale anomalies at the scale of the basin. However, there is an effect of compensation of the density of the sediments by an increased density in the underlying crust.

8. Basement depth from gravity inversion modelling

We estimated the depth of the basement from a preliminary gravity inversion modelling of the entire CB, using as input the gravity field *BG_RES1*, the seismic basement depth values along the seismic lines, and the superficial density contrast between the shallowest sedimentary layer and the crystalline crust. The top of the model is represented by the topography, the bottom by the top basement. The density of the basin is assumed to increase with depth, following an analytical parabolic function, which mimics the well-known exponential depth decay of rock porosity. The parabolic function represents the interpolation of the observed density increase as shown in Table 1. We performed the calculation imposing the maximum depth of the basement equal to 15 km (Delvaux et al., 2021). In particular, the density variation of the basin for increasing depths (Martins et al., 2010) is obtained using an analytic function that approximates the exponential compaction law. The function is the following:

$$\Delta\rho(z) = \frac{{\Delta\rho_0}^3}{(\Delta\rho_0 - \alpha z)^2} \tag{5}$$

with $\Delta\rho_0$, the superficial density contrast, and α the function parameter that governs the increase of density with depth (7). The increasing density is due to compaction and is expressed by an exponential function:

$$\Delta\rho(z) = \Delta\rho_0 e^{-\beta z} \tag{6}$$

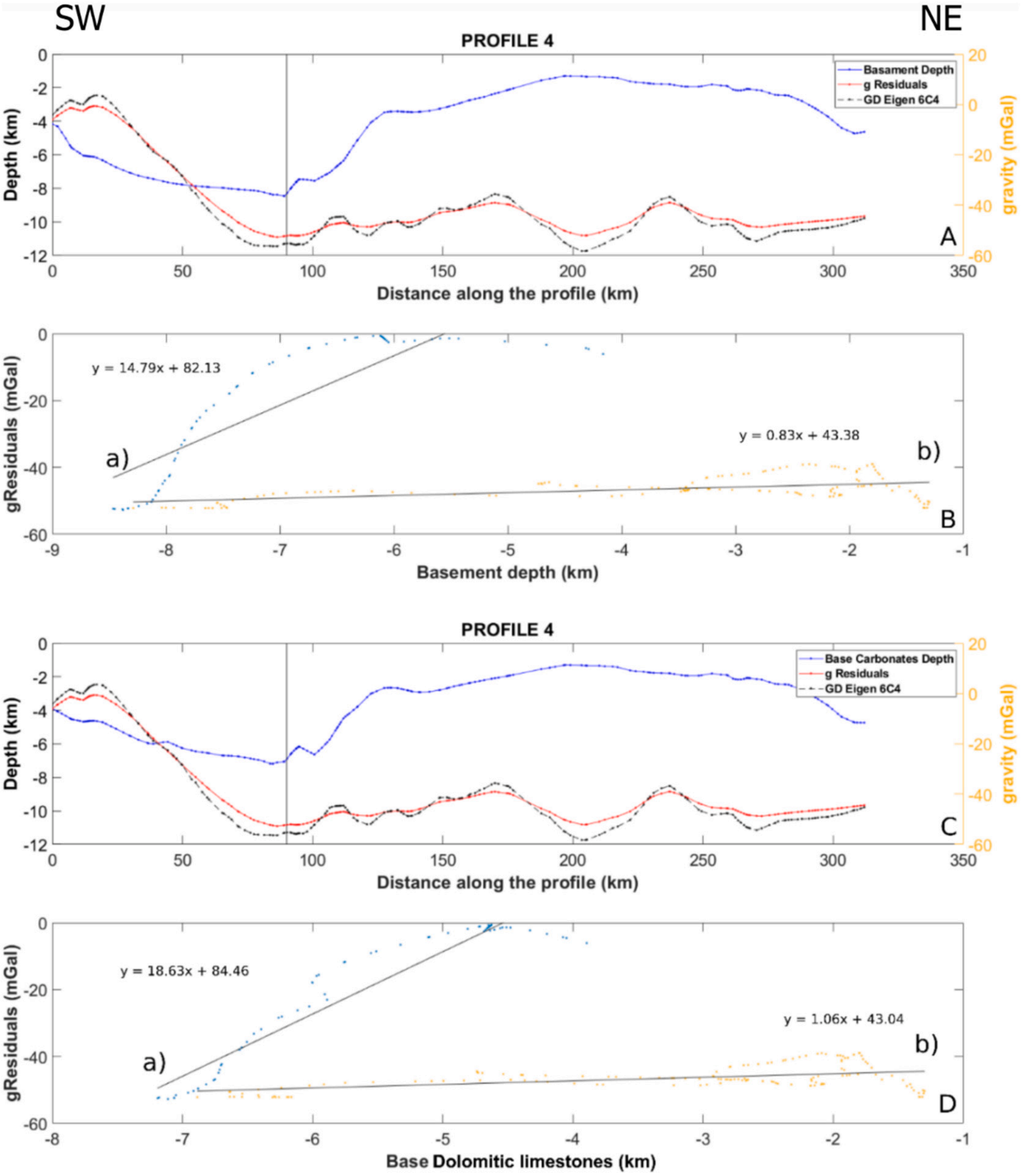

Fig. 12. Relationship between the residuals of the regression analysis, gravity disturbance, and depth of the seismic reflection horizons and scatter plot of the residuals of the regression analysis against the depth of the seismic reflection horizons along profile 4, displayed in Fig. 8. The vertical line shown in panels A and C represents the location, along the profile, in which the gravity data samples (panels B and D) change their trend. a) and b) labels refer to the two different lines interpolating samples referring to different tectonic structures present in the area crossed by the profile 4. In particular, the line a) describes the trend of samples in the Dekese Basin, while b) that of samples in the Lokonia High.

Table 3
Values of the correlation coefficients between the isostatically corrected Bouguer gravity anomalies (residuals of the topography-Bouguer field regression analysis) and depths of the crystalline basement (R0) and base of dolomitic limestones (R1), respectively, along the four profiles displayed in Fig. 8. In Profile 4, (a) and (b) values refer to the two different groups of samples showed in Fig. 12.

	Profile 1	Profile 2	Profile 3	Profile 4
Correlation Coefficient R0	0.723	0.297	0.832	0.916 (a) 0.237 (b)
Correlation Coefficient R1	0.785	0.423	0.906	0.909 (a) 0.241 (b)

where $\Delta\rho_0$ is the superficial density contrast and β the porosity decay parameter, assumed equal to 0.27 km^{-1}, which is a suitable value for sandstone (Allen and Allen, 2005), the most representative lithology of the CB sediments (Table 1). Given a reference depth (z_ref), chosen as maximum depth of the basement (15 km), we can calculate the parabolic parameter α:

$$\alpha = \frac{1}{z}\Delta\rho_0\left(1 - e^{\frac{1}{2}\beta z\_\text{ref}}\right) \tag{7}$$

This method based on the parabolic density estimation allows us to calculate the best approximation of the parabolic function to a given exponential function.

The results obtained by these first inverted tests (SM-Fig. 2) show a

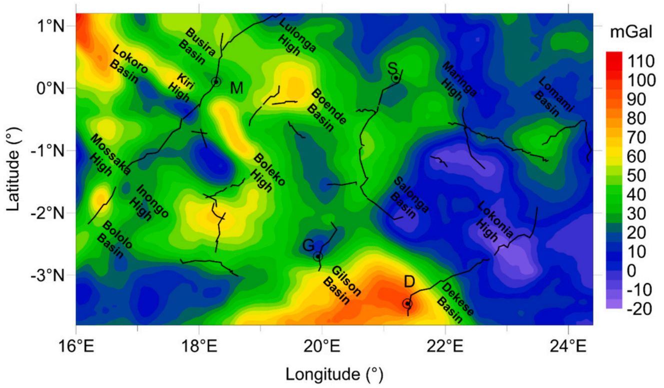

Fig. 13. Gravity residuals BG_RES2 obtained by subtracting the gravity effect of the sediments (G_SED) from the Bouguer residual values BG_RES1. Broken black lines show location of the seismic reflection profiles. Black circles show location of four wells drilled in the study area: D = Dekese; G = Gilson-1; M = Mbandaka-1; S = Samba.

basement depth shallower by several km compared to the seismic basement (Delvaux et al., 2021). This can be the effect of high-density bodies at crustal level below the basin, which partly compensate the gravity field (low-density sediments). They should be the reason for the systematically positive gravity residuals that we found in *BG_RES2*. We postulate the existence of these high-density bodies based on the observations of the broad gravity positive anomaly of these residuals (Fig. 13). In order to improve the consistency of the results obtained from the gravity inversion and the seismic interpretation, we first interpolated the residuals *BG_RES2* with polynomial regression surfaces (*PS*, linear, quadratic, and cubic, Fig. 14). To this purpose, we used SURFER software (Golden Software package), with the same size (Lat: -1.2°N-3.8°S, Lon: 16°E 24.5°E) and resolution (0.025°) of *BG_RES1*. In the case of cubic fitting, the long period correction amount to −35 mGal, while for the linear and quadratic the effect is lower. Afterwards, we subtracted *PS* from the residuals of the regression analysis *BG_RES1* (Fig. 8) and obtained *BG_RES3*, representing the sediments contribution. Indeed, although the interpolated basement has short-wavelengths flaws, it is a valid means to define the long-wavelength gravity field generated by the mantle and that remains after correcting the observed gravity field for crustal thickness and interpolated sediments. If this step would not be done, the gravity residuals corrected for the crustal thickness only, would still have a long wavelength signal, similar to an almost static shift, that does not represent the sediment layers or intra-crustal anomalies, which in turn produce shorter wavelengths.

The new residuals (*BG_RES3*, Fig. 14 A–C) are thus obtained subtracting the polynomial regression surfaces of first, second and third order. They show a similar distribution: the greatest negative values (<-80 mGal) coincide with the deep basins, while the weak negative or positive values correspond to the highs (Fig. 2). We observe that significant negative values are present also in regions uncovered by seismic data (such as those southwest to the Gilson Basin), which may identify other sedimentary depocenters along the margin of the Kasaï craton. We also notice that the increase of the polynomial degree causes an increase of the residuals range (Fig. 14 A–C). We invert *BG_RES3*, for the depth of the basement initially using a superficial density contrast of sediments against the crystalline rock basement of -0.400 g/cm^3 (SM-Fig. 3, SM-Fig. 4, Fig. 16A) and the above-mentioned parabolic density-depth curve (SM-Fig. 5). We then analyze the results along the four profiles used in the previous analyses (Fig. 15).

We can notice that the results do not change significantly by varying the polynomial degree of the surface (on average few hundred meters). However, the residuals obtained using the cubic surface (Fig. 14C) produce a basement depth slightly more consistent with the seismic basement (e.g., profile 4, Fig. 15).

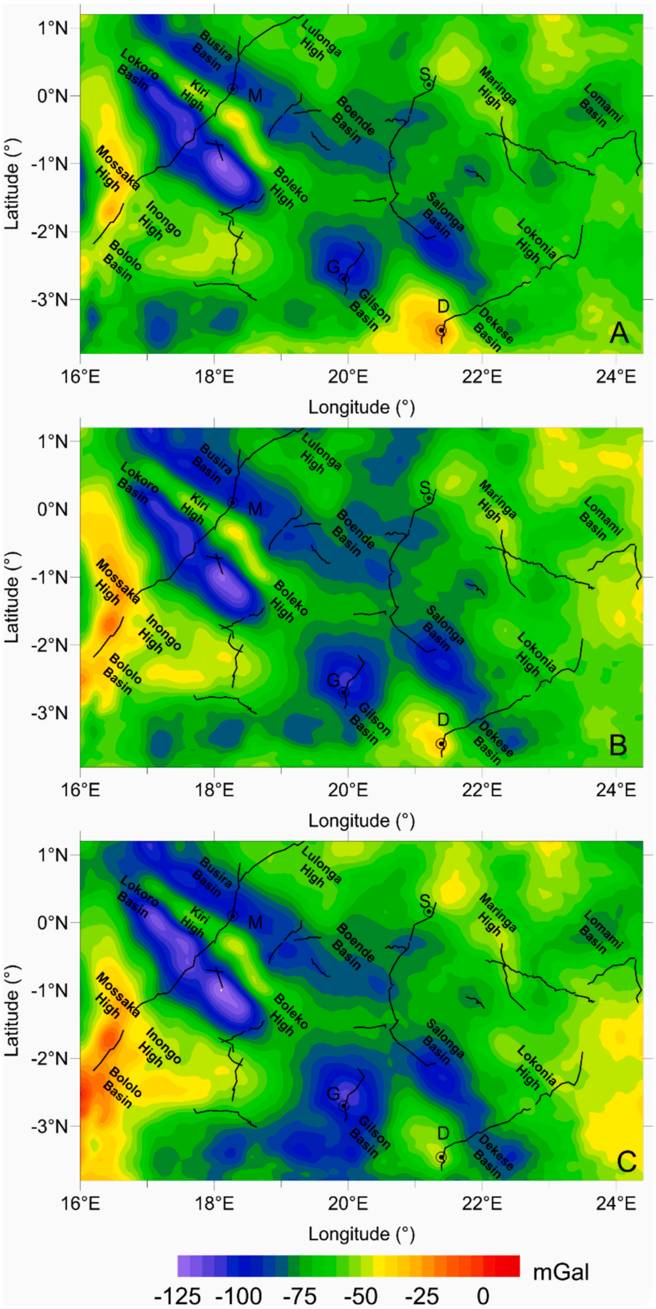

Fig. 14. Residuals (BG_RES3) obtained subtracting the polynomial regression surfaces: (A) Simple planar, (B) quadratic, and (C) cubic from the residuals BG_RES1 (Fig. 13). Broken black lines show location of the seismic reflection profiles. Black circles show location of four wells drilled in the study area: D = Dekese; G = Gilson-1; M = Mbandaka-1; S = Samba.

The comparison of the values of *G_SED* (Fig. 7), *BG_RES1* (Fig. 8), and the residuals *BG_RES3*, (Fig. 14 C) along the same four profiles (Fig. 17), shows that the first two fields have very similar trends, but only the last one is in the same range of *G_SED* (Fig. 7). This means that the residuals *BG_RES3* reflect only the effect of sediments. Furthermore, we notice a significant lateral variation of *G_SED* and *BG_RES3*, linked to the basement heterogeneity (high correlation between the negative anomalies and deep basins). Therefore, we considered for discussion only the results obtained from the inversion of the residuals *BG_RES3*, derived from the subtraction of the cubic polynomial surface (Fig. 14 C) and we

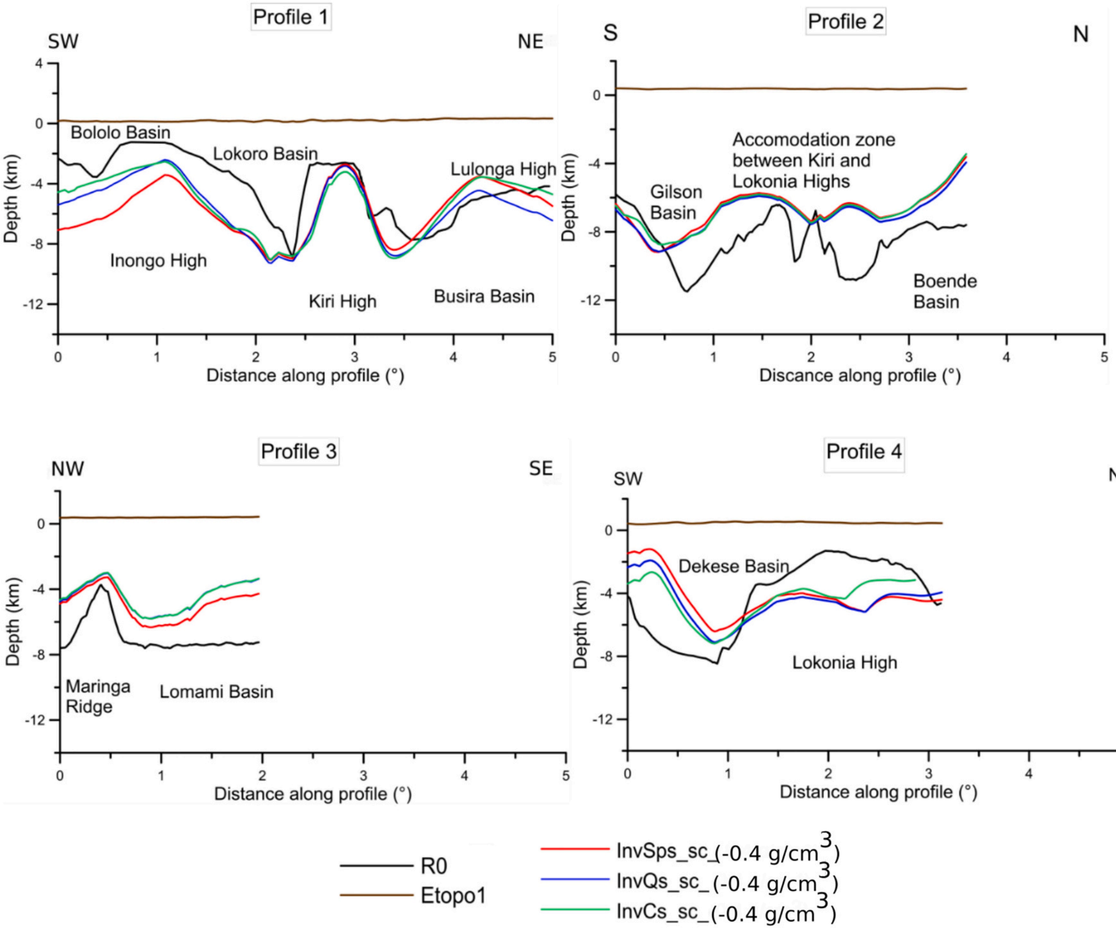

Fig. 15. Basement depth along seismic profiles displayed in Fig. 8, obtained from the inversion of the residuals displayed in Fig. 14, using seismic data as constraints and a density contrast between sediments and crystalline rock of −0.400 g/cm^3. Abbreviations in the legend are as follows: R0 = seismic basement. Etopo1 = topography. InvSps_sc(−0.4 g/cm^3) = Basement depth obtained for the inversion of the residuals BG_RES3 displayed in Fig. 14 A. InvQs_sc_(−0.4 g/cm^3) = Basement depth obtained for the inversion of the residuals displayed in Fig. 14 B. InvCs_sc_(−0.4 g/cm^3) = Basement depth obtained for the inversion of the residuals displayed in Fig. 14 C.

inverted them also using a starting superficial density contrast of −0.800 g/cm^3 (Fig. 16B). The choice of two different density contrasts was made, considering that the sedimentary layers have a different density and thickness in the study area (Delvaux et al., 2021). A very high density contrast (−0.800 g/cm^3) is justified, considering the very low density of the shallowest sediments (Table 1) and that of the rock basement in case its composition becomes more mafic for the intrusion of volcanic bodies (2.8 to 3.0 g/cm^3).

In defining the parabolic density increase, we find that in the range between −0.400 and − 0.800 g/cm^3, the density values obtained from samples can be fitted by the parabolic curve, but using the higher superficial starting density contrast, we observe a faster reduction of density contrast with depth (SM-Fig. 5). More precisely, from the top to the depth of 3 km, the density curve referring to the lower density contrast (Lower Density Curve, LDC), in SM-Fig. 5, shows a smaller density contrast associated to the basement depth, with respect to the other curve (Higher Density Curve, HDC). The opposite is true for depths greater than 3 km. The greatest density contrast produces a significant deepening of the basement depth in the basin areas, while in other parts this deepening is less evident (Fig. 16B). The results of the inversions using the two superficial density contrasts are displayed in Fig. 16 A–B and discussed in Section 10, together with those obtained from another gravity method described in Section 9.

9. Basement depths based on the analysis of the decompensative gravity anomalies

In the previous section, we derived the basement depth from the inversion of gravity residuals, obtained with a largely a-parametric reduction method. In this section, we present a complementary gravity method to obtain the depth of the basement. Indeed, the previous method determines the crustal contribution to the gravity observations by a data driven approach, while the method described here determines the same, using an isostatic compensation model that takes into account the rigidity of the lithosphere. The motivation to show the results of both methods is that a-priori preference to one or the other method is not possible without further constraints, and the comparison of the results from the two methods allows determining the inherent uncertainties, originating from the choice of one or other method. We start from the consideration that one of the main problems with the use of the gravity field for investigating the sedimentary cover is that the gravity effect of sediments might be substantially reduced, since these density anomalies are also isostatically compensated by deep masses and by elastic deformation of the lithosphere (Cordell et al., 1991). Kaban et al. (2021) has demonstrated that this reduction may reach one order of magnitude for extended basins. It has been suggested to restore the full effect of the upper crust and, in particularly, sediments by calculating a decompensative correction, which should be applied to the isostatic anomalies of the gravity field (Zorin et al., 1985; Cordell et al., 1991). This method

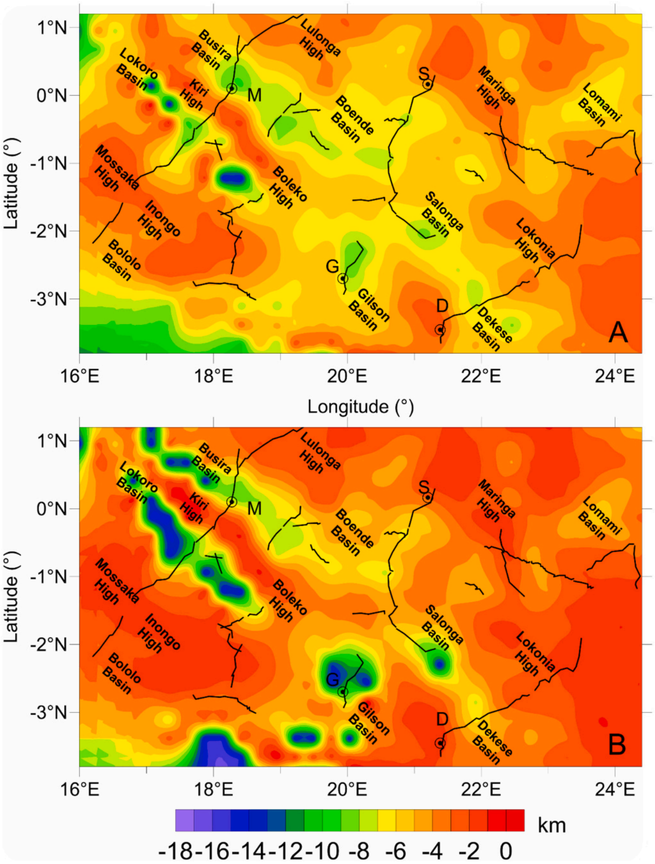

Fig. 16. Basement depth obtained from the inversion of the residuals (BG_RES3) displayed in Fig. 14C and constrained by seismic data. The shallow density contrast used is (A): -0.400 g/cm^3 and (B): -0.800 g/cm^3, with contrast decaying with depth according to the parabolic function. Broken black lines show location of the seismic profiles. Black circles show location of four wells drilled in the study area: D = Dekese; G = Gilson-1; M = Mbandaka-1; S = Samba.

has been successfully employed then in many previous studies (e.g. Cordell et al., 1991; Hildenbrand et al., 1996; Wilson et al., 2005). These authors have used only a local isostatic compensation scheme (Airy). Kaban et al. (2017) demonstrated that ignoring elastic deformation of the lithosphere might significantly bias the results. Later on, Kaban et al. (2017) and Haeger and Kaban (2019) have improved this method to account for the effective elastic thickness (*EET*) of the lithosphere. In the spectral domain, the correction applied to the isostatic anomalies (Δg_i (k_x, ky)) is computed as the follows:

$$\Delta gdc\ (kx,ky)=\frac{1}{exp(k\bullet M)/C-1}\cdot\Delta gi(kx,ky) \tag{8}$$

where M is the depth to the Moho, $k=\sqrt{k_x^2+k_y^2}$ is the wavenumber, $k_x = 2\pi/\lambda_x$ and $k_y = 2\pi/\lambda_y$. The parameter C controls the effect of regional compensation ($C = 1$ for the local one) and depends on the wavenumber and EET (T_e) (e.g. Turcotte and Schubert, 1982):

$$C=\Delta\rho g/\left(k^4D+\Delta\rho g\right) \tag{9}$$

where $D = ET_e{}^3/[12(1-\nu^2)]$ is the flexural rigidity, E is the Young modulus, ν is the Poisson ratio, $\Delta\rho$ is the average difference of the density of the topography and upper mantle material, and g is the gravitational acceleration.

The decompensative gravity anomalies (Fig. 18) have been computed for the entire CB in the previous study of Kaban et al. (2021). In that study, the thickness of sediments has been determined by using a predefined density-depth relationship based on four deep well logs. In the present study, we employ all existing seismic profiles to calibrate the relation between the decompensative gravity anomalies and thickness of sediments. The long-wavelength component is removed from the decompensative anomalies by applying a Gauss-type filter with the boundary wavelength 2500 km (Kaban et al., 2021) and thus their average level is equal to zero. However, the actual gravity effect of the upper crust should be negative due to low-density sediments, while the average density variations within the upper crystalline crust are assumed to be close to zero (Haeger and Kaban, 2019). These authors suggested to shift the decompensative anomalies downwards by a constant value, which can be determined based on well-studied areas. The average level of the effect of sediments turns to be very stable and varies around -15 mGal for different continents (Haeger and Kaban, 2019). For example, for Australia, where sedimentary basins have been studied in detail, this shift is equal to -14.6 mGal (Tesauro et al., 2020). Therefore, the decompensative anomalies, calculated for Africa, have been also reduced by 15 mGal before interpretation.

The density depth relation is non-linear for most of basins with a fast increase at shallow layers and more gradual after the depth 3–5 km. Stolk et al. (2013) and Finger et al. (2021) suggested approximating it with the function:

$$\rho_s(x)=\rho_{max}-(\rho_{max}-\rho_{min})exp(-Bx) \tag{10}$$

where $\rho_{max} = 2.75$ g/cm^3, $\rho_{min} = 2.03$ g/cm^3 (Table 1) and B is the coefficient, which controls the increase rate of the density and thus it represents the sediments compaction. B is relatively low for soft (low-density) basins and vice versa. This parameter has been determined from a statistical comparison of the decompensative gravity anomalies with the existing seismic determinations (the Root Mean Square, *RMS*, of the difference between calculated and observed values should be minimal). For the whole area, B is equal to 0.45 km^{-1} with the *RMS* of the difference between the predicted and observed thickness equal to 2.34 km. The histogram of these differences is shown in Fig. 19. It is clear that the underestimated values dominate (the difference is negative) and thus the mode value is slightly shifted below zero (Fig. 19). This could be expected since the lower layers of sediments are usually not so different in density from the crystalline rocks; therefore, their predicted thickness is more uncertain for deep basins (Haeger and Kaban, 2019).

Furthermore, the analysis in a sliding window with a radius of 1° has been performed to determine spatial variations of B for the area covered by seismic profiles (Fig. 20). This result is used then for calculation of the sedimentary thickness. For the area without seismic determinations we assume the average value $B = 0.45$ km^{-1}. To provide a smooth transition, the values were interpolated in the 1° band around the area with seismic data.

For a *variable B* value, the standard deviation from the observed values is reduced to 1.8 km compared to that of *constant B*, although local difference might be much higher. The differences' histogram is centered on zero, which demonstrates that this approximation is more reliable, although large negative deviations are still present. Considering the boundary limit of 10 points, all deviations are within ±2.5 km, which is close to the computed *RMS*. This value can be considered as a proxy of the determination error, although underestimations that are more significant are still possible. The final basement depth of the CB is shown in Fig. 21.

Comparing the parabolic density curve constructed on the base of the density function used here (Stolk Density Curve (SDC), SM-Fig. 5, with the other two curves discussed in previous section (Lower Density Curve, LDC) and Higher Density Curve, HDC), we can notice a strong similarity of the HDC curve up to 2 km. Nevertheless, the SDC curve shows a greater decrease in density contrast in depth than the others, mimic a clay-like rapid compaction (Allen and Allen, 2005). This makes this curve less realistic, considering that the CB stratigraphy is devoid of clay

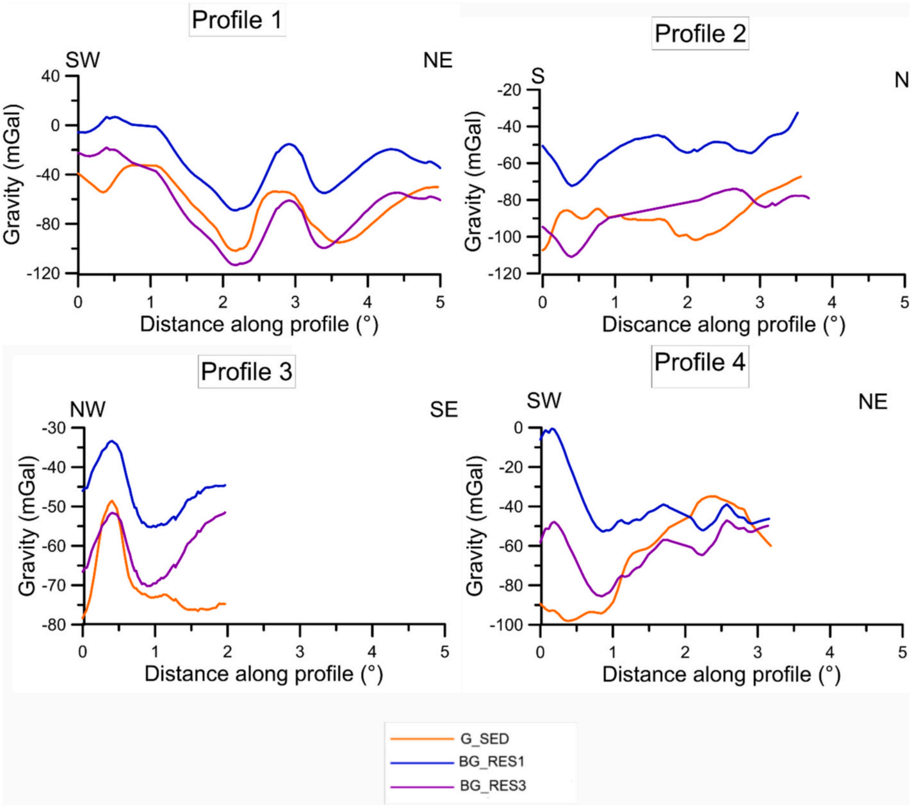

Fig. 17. Gravity fields along four seismic profiles displayed in Fig. 8. G_SED: Gravity effect of the sediments filling the seismic interpolated basement depth; BG_RES1: residuals obtained from regression analysis; BG_RES3: remaining signal after subtracting the polynomial (Cubic) surface from the field outcome of the regression analysis (BG_RES1).

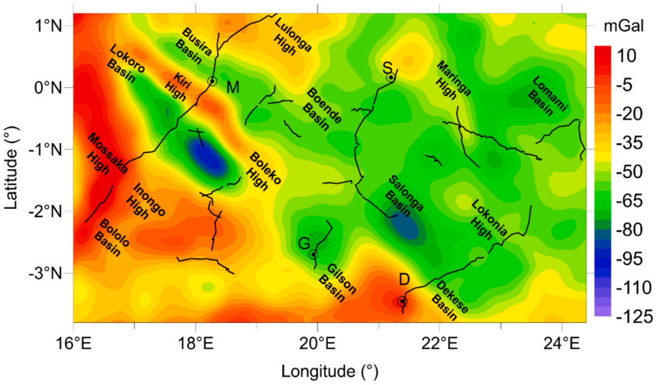

Fig. 18. Decompensative gravity anomalies of the gravity field (Kaban et al., 2021). Broken black lines show location of the seismic reflection profiles. Black circles show location of four wells drilled in the study area: D = Dekese; G = Gilson-1; M = Mbandaka-1; S = Samba.

formations. On the other hand, the standard deviation of the SDC with respect to the values of the well log data shows an intermediate value (0.129 g/cm^3), compared to those of the other two curves (HDC: 0.118 g/cm^3 and LDC:172 g/cm^3).

10. Results

The results, obtained using two gravity methods, show similarities and discrepancies, consequences of the different assumptions and parameters taken. First, we should consider that, as we discussed in

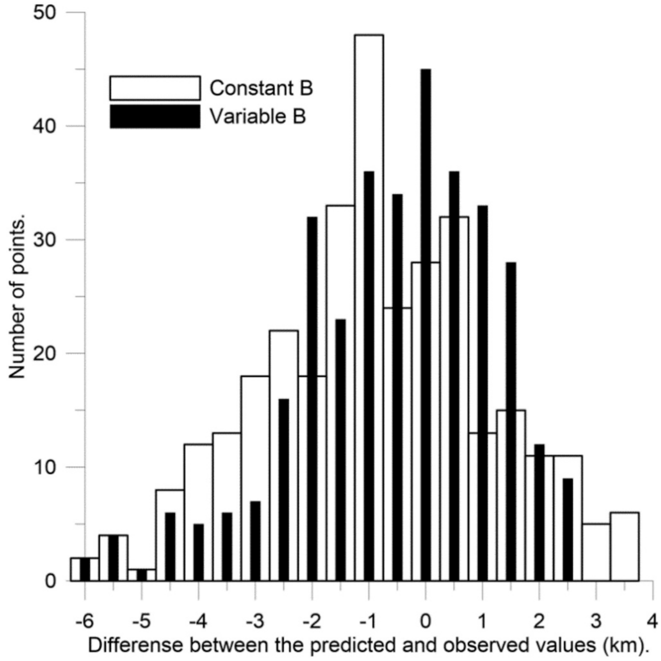

Fig. 19. Histograms of the differences between the predicted and observed thickness of sediments. Open bars show distribution for the constant B and solid ones for the variable B.

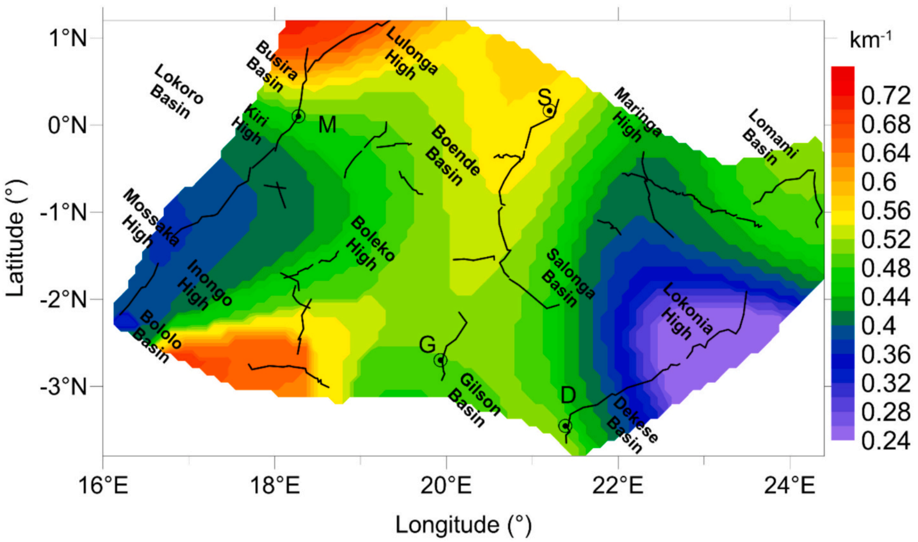

Fig. 20. Parameter B determined in a sliding window by comparing the decompensative gravity anomalies and seismic data on the sedimentary thickness. Broken black lines show location of the seismic reflection profiles. Black circles show location of four wells drilled in the study area: D = Dekese; G = Gilson-1; M = Mbandaka-1; S = Samba.

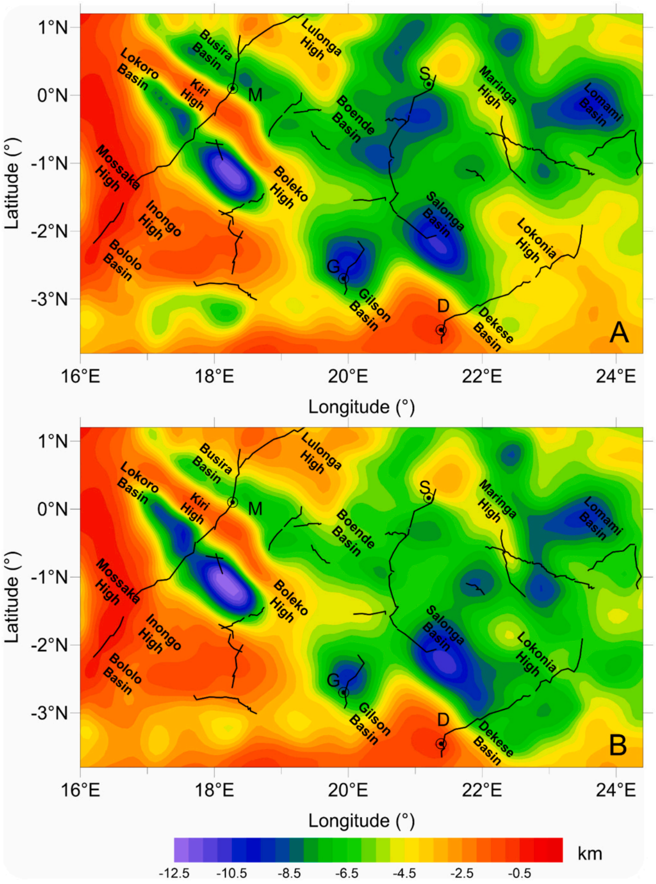

Fig. 21. Depth of the basement determined from the decompensative gravity anomalies. (A): For a variable B. (B): For a constant B = 0.45. Broken black lines show location of the seismic reflection profiles. Black circles show location of four wells drilled in the study area: D = Dekese; G = Gilson-1; M = Mbandaka-1; S = Samba.

previous section, both decompensative anomalies and gravity residuals *BG_RES3* (Figs. 18 and 14C) are mostly induced by the density variations of sediments, and much less by those of the underlying crystalline crust. This makes these two fields comparable. To this purpose, we can notice that both maps of these anomalies (Figs. 18 and 14C) show negative peaks exceeding −100 mGal in some common areas (southern Lokoro Basin), although *BG_RES3* shows much larger negative values in the southern sectors of the CB, reaching approximately −125 mGal near the Gilson well. Furthermore, both fields show positive values along Inongo and Mossaka highs. The consistency of the results can confirm the absence of very dense intrusive geological bodies in the Bololo, Mossaka, and Inongo High structures. Moreover, in the southeastern sector of the CB (corresponding to the seismic profile 4), we notice in *BG_RES3* (Fig. 14C) a negative trend around −90 mGal, which connects the Salonga with the Dekese Basin, while the decompensative gravity anomalies (Fig. 18) show only a negative peak (-85mGal) at the Salonga basin. Since there are no seismic profiles that intercept the area, it is difficult to demonstrate which result is the most reliable. Nevertheless, it is evident from both maps (Figs. 18 and 14C) that from the Dekese well to the northeast, along profile 4, there exists an alternation of structural highs and lows until Lokonia High. They correspond to weak negative gravity anomalies (up to −50 mGal in both maps) and stronger negative anomalies at the Dekese Basin (about −70 mGal in Fig. 18 and −85 mGal in Fig. 14C). The comparison between the seismic basement depths with those based on gravity analyses shows the existence of common features. In particular, we can identify three main deep depocenters, where the basement reaches very large depths (between 9 and 11 km, according to the seismic basement, and between 7 and 16 km, based on gravity analyses): the Lokoro Basin in the SW and two basins, such as the Gilson and Boende, NE-SW oriented. The Lokoro Basin, formed by two main NW-SE trending depocenters, with its maximum depocenter lying in areas uncovered by seismic profiles, is separated from the Busira Basin (maximum basement depth about 7.5 km) by the Kiri High. The deepest depocenters of the Lokoro and Gilson basins, detected from gravity, are shifted southeast and south, respectively, with respect to the maxima shown in the seismic basement (Fig. 2). The deepest depocenter of the Lokoro Basin lies in an area uncovered by seismic profiles (Figs. 16 and 21). Furthermore, the gravity basement depths show other basins, one in the northeastern sector of the CB, the Lomami Basin, NW shifted with respect to that obtained from the interpretation of seismic profiles (Fig. 2), and some others southeast to the Gilson Basin. The last ones are

Table 4
Correlation coefficient (CC) between the different basement depth maps. R0: seismic basement. Inv400 and Inv800: basement depth obtained from the inversion of the gravity residuals BG_RES3, using a density contrast value of -0.400 g/cm^3 and $-$ 0.800 g/cm^3, respectively. ConstantB and VariableB: basement depth obtained from decompensative gravity anomaly method, using B = 0.45 and variable B value, respectively.

	R0	Inv400	Inv800	ConstantB	VariableB
R0	1.000	0.242	0.254	0.501	0.661
Inv400	0.242	1.000	0.698	0.289	0.390
Inv800	0.254	0.698	1.000	0.318	0.397
ConstantB	0.501	0.289	0.318	1.000	0.913
VariableB	0.661	0.390	0.397	0.913	1.000

observed only from the inversion of the gravity residuals, when we used the greatest superficial density contrast (-0.800 g/cm^3). Indeed, we can notice that when we use this value, the depth of the basement becomes deeper and shallower by about 2–3 km in the basins and areas outside, with respect to the values provided by the seismic profiles (Fig. 2). In addition, the basins appear more laterally extended, as in the case of the Busira Basin, which is elongated in NW direction (Fig. 16B). The enigmatic Salonga Basin, having a peculiar position, in the alignment of the Kiri High and highlighted by a positive magnetic anomaly, is identified only by the basement depths reconstructed from gravity modelling (Figs. 16 and 21). From the basement depth obtained from the interpolation of seismic profiles, it merges with the Gilson and Dekese basins in one single large sedimentary depocenter (Fig. 2).

The basement depths derived from decompensative anomalies, using a variable and constant *B* value (Fig. 21), show a similar distribution of depocenters. The last ones reach a greater depth for a variable *B* (Fig. 21A) (up to 10 km), than when we consider a constant *B* value (Fig. 21B) in the Lokoro, Salonga, and Lomami basins, while the opposite is true in the Busira, Boende, and Gilson basins. It should be noted that both maps are quantitatively different from the map presented in Kaban et al. (2021), although the main patterns (shape of local basins) are similar, and have values more consistent with those of the seismic basement (Fig. 2). This confirms the importance of the calibration with the existing seismic determinations. Therefore, by analyzing the gravity fields, using the seismic data as constraints, we have been able to recover the basement depths in the CB with higher accuracy in the area between the seismic profiles, suppressing the artefacts due to their interpolation. The basement depths obtained from the two gravity methods (Figs. 16 and 21) show an alternation of basins and highs, NW-SE trending (Fig. 16 A–B), which is not clearly visible looking at the seismic basement depths. The Kiri High matches the highly axial magnetic zone, which is marked by the general absence of dolomitic limestones, dividing the central area of the CB into two parts. The continuity of the Kiri High, masked by the effect of the interpolation of the seismic profiles (Fig. 2) and the sharp transition to the surrounding deep basins is enhanced when we use the superficial density contrast of -0.800 g/cm^3 (Fig. 16B). The correlation coefficient between the different gravity

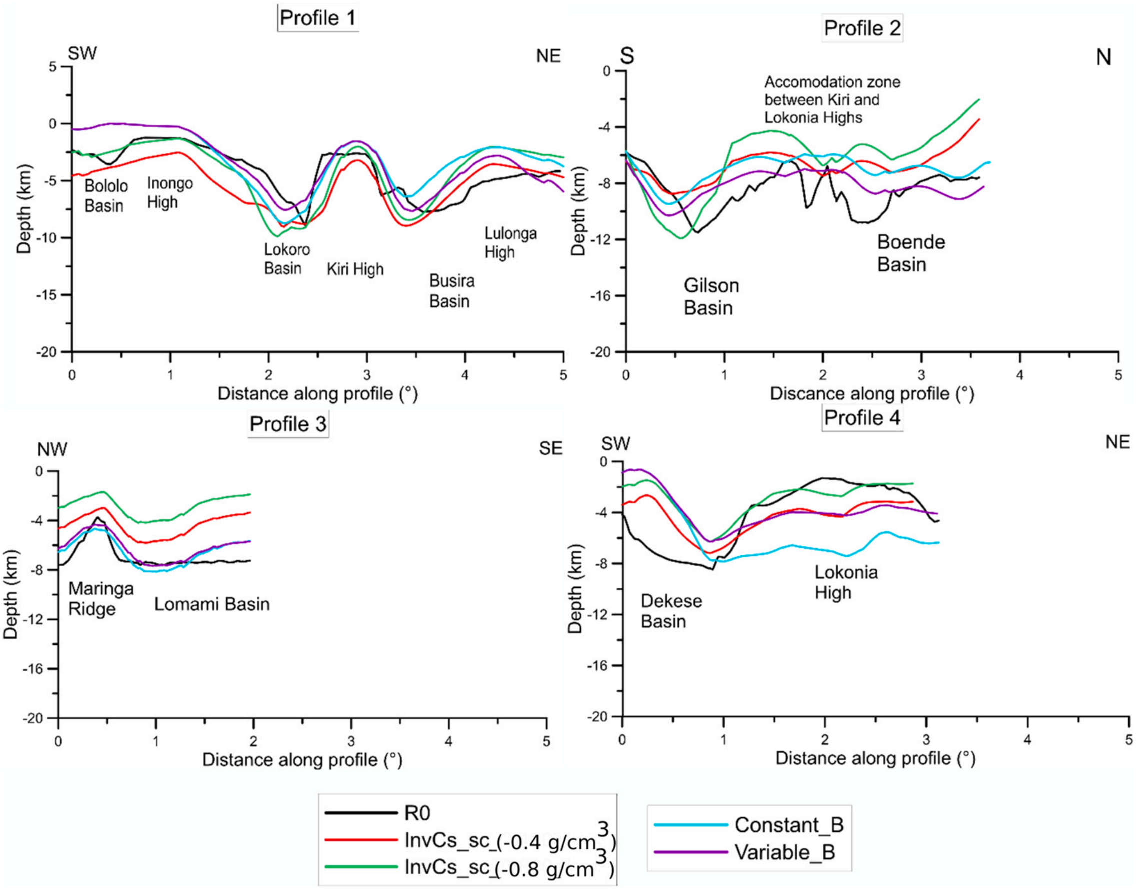

Fig. 22. Comparison between all the methods used for the investigation of the basement depth along four seismic profiles displayed in Fig. 8. R0: basement depth obtained from interpretation of seismic reflection profiles; InvCs_sc_0.4 g/cm: basement depth obtained from gravity inversion using a density contrast of -0.400 g/cm^3. InvCs_sc_0.8 g/cm: basement depth obtained from gravity inversion using a density contrast of -0.800 g/cm^3. Constant_B: basement depth derived from decompensative gravity anomaly method, assuming constant value of B. Variable_B: basement depth derived from decompensative gravity anomaly method, assuming a variable value of B.

basement maps, as expected, reveals a significant consistency between the results obtained using the same method, while it is relatively weak in all the other cases (Table 4). This is not surprising, considering that the gravity basements have been constrained by the seismic data that cover a little part of the study area (Fig. 1). Therefore, the greatest correlation coefficient with the seismic basement is equal to 0.661, given by the basement depth obtained from the decompensative anomalies using a *variable B* (Table 4).

The weakness of the correlation coefficients between the results obtained from the two methods can be partly ascribed to the different density-depth function used, parabolic for the inversion modelling and exponential in the decompensative approach. We should also consider that the seismic data constrain the gravity inversion, while calibrate the decompensative anomalies and that a different basement density contrast was used (2.67 g/cm^3 in the gravity inversion method and 2.75 g/cm^3 in that based on inversion of decompensative anomalies). Furthermore, to obtain the basement depth from the decompensative anomalies, rigidity of the lithosphere has been taken into account, while the first gravity method is aparametric for retrieving the crustal isostatic contribution and uses polynomial surfaces to smooth gravity signals, associated with deep tectonic structures. To compare the results in more detail, we derived the seismic (Fig. 2) and gravity basement depths along the four profiles (Fig. 22) used in the previous analysis (Sections 7 and 8).

Along profile 1, the basement depths obtained from the gravity data show similar trends and reproduce more smoothly the seismic basement depth variations and thus they do not identify sharp transitions between local sedimentary deeps and highs (Fig. 22). The maximum misfit of all gravity basement depths with respect to the seismic one is about 2–3 km. This indicates that the different methods produce consistent results and support the interpretations of the seismic reflection profiles. The correlation coefficients (*CC*) between the seismic and gravity basement depths along the profile are high, reaching values between 0.737 and 0.728 and even higher between the different gravity basement depths ($CC = 0.972$) (SM-Table1). The basement depths obtained from the decompensative anomalies with variable *B* is in general shallower than the others are. Lokoro Basin and Kiri High are well identified by the variation of all basement depths, which predict for the former a maximum depocenter between 8 and 12 km (Fig. 22). The maximum depth of the Busira Basin, reconstructed from the gravity inversion, is southwestward shifted by some tens of kilometers with respect to that obtained from seismic interpolation (Section 7) and decompensative anomalies. On the other hand, the shallow Bololo Basin and Inongo High are not clearly distinguished by the trend of the gravity basement depths. The last ones are 2–3 km shallower than the seismic basement in the Lulonga High. This feature likely indicates that the density of sediments has been locally underestimated or can be related to the crustal effect not completely removed, considering that the residuals reflecting the crustal density variations (Fig. 12) are strongly positive (~70 mGal).

Along profile 2, all the gravity basements are poorly correlated with the seismic basement ($CC < 0.5$), but the correlation is much higher when we compare the results obtained from the different gravity methods (SM-Table2). The discrepancy between the results obtained with different gravity methods and seismic basement depth, in the area representing the accommodation zone between the Kiri and Lokonia High, can be partly ascribed to the strong lateral heterogeneity of the seismic basement, which is highly faulted (Delvaux et al., 2021). The basement depths obtained from the gravity inversion (red and green lines in Fig. 22) and decompensative anomalies (Fig. 22) clearly identify the Gilson Basin, but its maximum depth is southward shifted, with respect to the results based on seismic data (Fig. 2). This part of the seismic profile is also very faulted and heterogeneous, with many gaps that make the interpretation more difficult (Delvaux et al., 2021). We can further notice that the higher density contrast (−0.800 g/cm^3) produces a basement depth more consistent with the seismic basement in the areas where the intermediate and low-density sediments have a thickness significantly greater (6–8 km) than that of the underlying carbonate sequences (1–2 km). This mostly occurs in the basins located in the southern part of the CB (e.g., Bololo and Gilson basins, profile 1 and 2, Fig. 22).

Along profile 3, the relatively high correlation coefficients between the seismic basement depth and that obtained from gravity data (max $CC = 0.776$, Supplementary material SM-Table3), indicates their good consistency. As in the previous cases, the correlation coefficients are even higher when we compared the different gravity methods among each other. Indeed, the trends of the basement depths obtained from gravity data are very similar, but the values are quite different (Fig. 22). In particular, we can observe that the basement depths obtained from the two inversion modelling methods, using a superficial density contrast of −0.800 g/cm^3 and − 0.400 g/cm^3 (InvCs_sc_-0.8 g/cm^3 and InvCs_sc_-0.4 g/cm^3), are shallower than the seismic basement by up to 4–5 km. The depths obtained from the decompensative anomalies show more consistency with the seismic data. Along this profile, a smaller density contrast (−0.200 g/cm^3) in the gravity inversion would improve the consistency with the seismic basement depth. The reasons could be that the thickness of Proterozoic clastics and Dolomitic limestones (Tables 1 and 3) is particularly high in the Lomami Basin (Delvaux et al., 2021). In that area, the seismic basement is sub-horizontal, while all the gravity methods produce trends that are more variable. In particular, the basement depths obtained from decompensative anomalies and inverted models (Fig. 22) tend to be shallower in the southeastern part of the profile. This can be ascribed by lateral density variations of the sediments and/or shallow crust, whose effect can be still present. The last hypothesis can be supported by the increase of the residual values displayed in Fig. 14, from about 20 mGal to 35 mGal, in the southeastern part of the profile.

Along profile 4, the correlation coefficient between the seismic basement depth and the results obtained from the inversion gravity modelling (Sections 7 and 8) is relatively high ($CC > 0.600$), indicating the good consistency between the trends (Fig. 22). On the other hand, the basement depths obtained from decompensative anomalies shows an opposite trend with respect to that of the seismic basement, producing a low correlation coefficient ($CC < 0.200$; SM-Table4). All the methods based on gravity data identify the Dekese Basin, with the maximum depth approximately coincident with that obtained from seismic data. However, in the south-westernmost part of the profile the basement depths based on decompensative anomalies and inversion modelling show a reverse trend to that observed in the seismic basement depth (Fig. 22). This can be explained by the effect of an anomalous high-density crust not completely removed. The presence of a high-density mass in this area (southernmost part from Dekese well) has been also postulated by the study of Watts et al. (2018), which observed sediment-corrected Bouguer gravity anomalies of about 50 mGal. This hypothesis is based on the presence of a strong positive anomaly of *BG_RES2* (~ 90 mGal, Fig. 13). In the Lokonia High, all the gravity basement depths show a trend very similar to that of the seismic basement (Fig. 22).

Potential uncertainties of the basement depths obtained from the inversion of the residuals *BG_RES3* arise from two major sources. First, we should consider that the depth of the seismic basement and other horizons, to constrain gravity calculations, could be affected by uncertainties, related to the seismic data acquisition, processing, and interpretation. Since a complete uncertainty analysis would only be possible with a Montecarlo simulation approach, which is out of the scope of this study, we tested the influence on the *G_SED* and basement depth of the uncertainty of the total sedimentary thickness. To this purpose, we introduced in the calculations a variation of ±10% (Fig. SM-Fig. 6) of each sedimentary layer thickness. Such a thickness variation produces a change of the *G_SED* values of about ±22 mGal (Fig. SM-Fig. 6C), which translated in an uncertainty of the basement depth obtained from gravity inversion of about ±1.5 km (Fig. SM-Fig. 7). Potential uncertainties of the basement layers based on the decompensative gravity anomalies arise from two sources. First, the density-depth relation could be quite different from a smooth curve used in this case. Second, some part of the decompensative anomalies could be induced by density variations within the uppermost crystalline crust, although the last ones are likely not as significant as for sediments. Kaban et al. (2021) pointed out that the error remarkably increases with sedimentary thickness, since the density difference of deep sedimentary layers with surrounding crystalline rocks is very small. This is also visible from the histogram in Fig. 19. For the depths less than 9 km, we can accept the value 2.5 km, which also corresponds to the *RMS* of the difference with the seismic determinations. For greater depths, it is hardly possible to quantify the error due to the abovementioned factor. Therefore, the results are rather qualitative than quantitative for the deepest parts of the CB.

11. Discussion

The comparison made in the previous section between the results obtained from two different gravity methods, each of them using two different assumptions, revealed that the CB has a very heterogeneous basement, characterized by an alternation of highs and NW-SE oriented sedimentary depocenters (Figs. 16–20). The alignment of these structures coincides with the series of positive and negative Bouguer and free-air gravity anomalies (Fig. 6) and has been detected for the first time in Cahen (1954) and confirmed later by Kadima et al. (2011a and 2015), Buiter et al. (2012), and more recently by Kaban et al. (2021). However, the gravity analysis of Buiter et al. (2012) and Kadima et al. (2011a and 2015) did not provide a reconstruction of the basement depth. The basement depths derived from our gravity analyses reveal the continuity of the Kiri and Boleko highs, which is confirmed, besides by matching with the axial highly magnetic zone, also by their relatively high surface wave velocities and densities recently estimated in the study of Raveloson et al. (2021). The origin of the Kiri High has been highly debated, in order to explain its continuity. In the past it was thought to be the rift axis, successively inverted by the compressional tectonics (Daly et al., 1992; De Wit et al., 1992), while Kadima et al. (2011a, 2011b) highlighted the role that salt tectonics could play in creating this structure. Delvaux et al. (2021) confirmed that the Kiri High developed in the beginning of the history of the CB, appearing during the rifting stage, and that compressional reactivations occurred along its margins with the adjacent basins.

Our new basement depths clearly distinguish different depocenters within the CB (Figs. 16 and 20). In contrast, Linol et al. (2016) found a single depocenter with a maximum thickness of only 6 km, while the most recent surface wave velocity model of Raveloson et al. (2021) reveals the presence of two basins ~8 km deep, divided by the Kiri High. The presence of several basins identified in this study, having different shape and depth, is linked to the complex tectonic history of the CB. It led to the migration of the sedimentary depocenters from the Proterozoic to Jurassic and lateral thickness variations of the sedimentary layers, with a progressive decrease in the influence of the initial rift structures (Delvaux et al., 2021).

The initial rift phase produced stronger subsidence in the northern part of the CB, as observed by the greater thickness of the *syn*-rift sediments located in that part of the basin (Delvaux et al., 2021). On the other hand, the following compressional stress, related to the Gondwana assembly, enhanced the initial subsidence related to the rift extension, in the southern part, forming the deepest depocenters (>7 km) of the CB (Lokoro, Gilson, Bololo, and Dekese basins). Therefore, both the extensional and compressional phases might not have acted uniformly on the CB, but along different preferential directions. Following the Gondwana assembly, there have been only minor phases of tectonic stress accompanied by climatic changes that further modified the morphology of the CB. The succession of compressional events to a rift extension occurred also in other intracratonic basins, such as those of North America, producing significant variations in their subsidence trends and morphology (e.g., Klein and Hsui, 1987). Another example is given by the phases of intracontinental orogeny that lead to the separation of the Centralian Superbasin of Australia in four main basins (between 600 and 300 Myr), such as Officer, Amadeus, Ngalia, and Georgina basins (e.g., Lindsay, 2002). Furthermore, the study of Perron et al. (2018), using satellite images, geological, and potential field data, to characterize the basement of the basins lying on the African metacraton, revealed that these basins were coeval with the CB and their evolution has been influenced by some common tectonic and climatic processes (e.g., the Pan African collision).

The gravity models implemented in this study, gave us also the chance to make hypothesis about the crustal nature of the CB. In particular, we supposed the presence of small mafic bodies at crustal depths, in the southern part of the CB, in the Dekese Basin and surroundings, which could be responsible for the strong localized positive anomalies of the gravity field *BG_RES2*. We attributed the origin of these mafic bodies to the extensional tectonics that caused the CB formation. However, according to the seismic tomography of Ojo et al. (2020), the shear wave velocities are not very high in the lowermost part of the crust. For this reason, we suppose that the injection of mafic bodies would have occurred only sporadically and that most of the crust would not have been thinned during the extensional tectonics, since its current thickness (about 40 km, Ojo et al., 2020) is higher than what it would be in isostatic conditions (Finger et al., 2021). This is supported by the presence in the Mbuji-Maji Supergroup, deposited during the initial rifting stage of dense basaltic lavas and dolerites in the Mbuji-Maji area (Delvaux et al., 2021), in the southeast continuation of the Dekese and Salonga Basins (Fig. 4) They are found on top of the Mbuji-Maji Supergroup in the southwestern branch of the Mbuji-Maji basin, while they are present as a large planar intrusion in the middle of the Mbuji-Maji Supergroup in the northeastern branch. Alternatively, we can hypothesize the presence of a high-density lowermost crust, even if the last one has not been detected by the seismic tomography. Indeed, high-density minerals are not necessarily characterized by anomalous shear-wave velocities. In this case, the high-density anomalies of the *BG_RES2* residuals would be related to mafic bodies composing the lower crust.

We can also speculate that the asthenospheric upwelling induced by the extensional stress has metasomatized the lithospheric cratonic roots, producing weakening and densification of the original cratonic lithosphere. This process that probably caused a small erosion of the lithospheric roots, considering the present-day great lithospheric thickness (200–250 km, according to the seismic tomography model of Celli et al., 2020), could have enhanced the basin subsidence, initiated by the action of extensional stress. Further hypotheses that link the present-day structure of the CB to the tectonic processes, occurred during its history, and likely explain the origin of its huge negative free-air and geoid gravity anomaly, will be possible to put forward in the near future. Indeed, the deployment of more seismic stations in the African continent, through the ongoing African Array project (AfricaArray.psu.edu), offers the chance to increase our knowledge on the crustal and mantle structures of the CB.

12. Conclusions

We reconstructed the basements depth variations of the CB using two different gravity methods, augmented by all the geological and geophysical data available for the study area (e.g., seismic reflection profiles, well log, aeromagnetic data, and density measurements on rock samples). The first method retrieves the basement depth from inversion of gravity residuals (*BG_RES3*), obtained from the regression analysis between the surface topography and Bouguer gravity anomalies (*BG_RES1*), to which we subtracted a cubic polynomial surface, related to the crustal or sub crustal gravity effect (*BG_RES2*). This gravity method has been applied using two different density contrasts between that of the shallow sediments and crystalline crust (−0.400 and −0.800 g/cm^3, respectively). The other gravity method is based on the inversion of the decompensative anomalies, which takes into account the rigidity of the lithosphere and uses both a constant and a variable coefficient, controlling the increase rate of density with depth for the sediments.

The main results obtained are summarized below:

- Both gravity methods confirm the strong heterogeneity of the basement depths of the CB that, because of its long and complex geodynamic history appears composed of structural highs and lows NW-SE oriented, coinciding with the axial magnetic zone.
- The applied gravity methods allowed us to reconstruct the basement depths quite consistently with the values obtained from the interpretation of the seismic profiles and suppress the artefacts produced by the interpolation of the seismic data. Indeed, we were able to identify the continuity of the Kiri and Boleko highs that appeared in the reconstructed seismic basement separated by a sedimentary cover and clearly distinguish the Busira (7–9 km deep), Lokoro (10.5–12 km deep), and Salonga basins (10–11.5 km deep).
- The results of the gravity analyses, reveal the presence of the Lomami Basin (~11 km deep), in the areas uncovered by seismic data, in the northeastern sector of the CB. Other possible basins ~9 km deep, located southeast to the Gilson Basin, along the margin of the Kasaï Craton, have been identified only from gravity inversion using a superficial density contrast of -0.800 g/cm^3.
- The gravity effect of sediments is strong in the basins where the syn-rift sediments are thinner than those of the overlying sequences, having a lower density (Lokoro, Gilson, and Boende basins). In contrast, in other basins (Salonga and Lomami basins) the gravity effect of sediments is reduced because of the large thickness of the high-density syn-rift sequences (mostly carbonates and clastic sediments). These differences are likely responsible for the under or overestimation of the basement depths, derived from the inversion of the gravity residuals using the two different density contrasts.
- The comparison between the basement depths obtained from the different gravity methods with the seismic basement along the profiles shows that the major discrepancies (about 3–4 km) can be ascribed to the gravity resolution, not sufficient to detect the sharp lateral variations of the basement depth, occurring in the highly faulted zones.
- The analysis of the gravity anomalies mainly related to the crystalline crust (*BG_RES2*) reveals the possible presence of high-density bodies in the Kiri, Boleko, and Mossaka High and in the Dekese basin and surroundings, likely related to the rift phases that determined the formation of the CB.

Data sources

Aeromagnetic data provided by D. Fairhead (GETECH Group Plc., Kitson House, Elmete Hall, Leeds, LS8 2LJ, UK). The release of magnetic data from GETECH has been done in the frame of a scientific collaboration between the Royal Museum for Central Africa and GETECH. The seismic profiles have been obtained from the CNE, Kinshasa, and D.R. Congo thanks to S.M. Kabeya.

Declaration of Competing Interest

The authors declare that they have no known competing financial interests or personal relationships that could have appeared to influence the work reported in this paper.

Acknowledgements

A PhD grant to author Francesca Maddaloni was provided by Regione Friuli Venezia Giulia (Italy) through a European Social Fund (FSE) 50% cofounded fellowship. Magdala Tesauro acknowledges the grant "INTRAcratonic basins TECTOnic evolution: The Congo Basin (INTRA-TECTO)". We acknowledge the RMCA for the availability of seismic and geological data. Aeromagnetic data have been processed by M. Evraerts. We are grateful to Dr. Alberto Pastorutti and Tommaso Pivetta for helpful discussions, assistance in program coding and informatics system management. The comments of three anonymous reviewers have significantly improved a previous version of the manuscript.

Appendix A. Supplementary data

Supplementary data to this article can be found online at https://doi.org/10.1016/j.gloplacha.2021.103611.

References

Abdelsalaam, M.G., Liégeois, J.-P., Stern, R.J., 2002. The Sahara Metacraton. J. Afr. Earth Sci. 34, 119–136.

Allen, P.A., Allen, J.R., 2005. Basin Analysis. Blackwell Publishing, Oxford.

Amante, C., Eakins, B.W., 2009. ETOPO1 1 Arc-Minute Global Relief Model: Procedures. Data Sources and Analysis. NOAA Technical Memorandum NESDIS NGDC-24, 19 pp.

Barritt, S.D., 1983. The African magnetic mapping project. ITC Journal 2, 122–131.

Blakely, Richard J., 1995. Potential Theory in Gravity and Magnetic Applications. Cambridge University Press. https://doi.org/10.1017/CBO9780511549816.

Braitenberg, C., 2015. Exploration of tectonic structures with GOCE in Africa and across-continents. Int. J. Appl. Earth Obs. Geoinf. 35 (A), 88–95. https://doi.org/10.1016/j.jag.2014.01.013.

Braitenberg, C., Ebbing, J., 2009. The GRACE-satellite gravity and geoid fields in analysing large-scale, cratonic or intracratonic basins. Geophys. Prospect. 57, 559–571. ISSN: 0016-8025. https://doi.org/10.1111/j.1365-2478.2009.00793.x.

Buiter, S.J.H., Steinberger, B., Medvedev, S., Tetreault, J.L., 2012. Could the mantle have caused subsidence of the Congo Basin? Tectonophysics 514-517, 62–80.

Cahen, L., 1954. Géologie du Congo Belge. Vaillant-Caramane. Liège, 577pp (OCoLC) 594632320.

Cahen, L., 1983a. Brèves précisions sur l'âge des groupes crétaciques post-Wealdien (Loia, Bokungu, Kwango) du Bassin intérieur du Congo (République du Zaïre). In: Rapport annuel du Musée Royal de l'Afrique centrale, Tervuren (Belgique). Département de Géologie et de Minéralogie, pp. 61–72.

Cahen, L., 1983b. Le Groupe de Stanleyville (Jurassique supérieur et Wealdien de l'intérieur de la République du Zaïre): Révision des connaissances. In: Rapport annuel du Musée Royal de l'Afrique centrale, Tervuren (Belgique). Département de Géologie et de Minéralogie, pp. 73–91.

Cahen, L., Ferrand, J.J., Haarsma, M.J.F., Lepersonne, J., Verbeek, Th., 1959. Description du sondage de Samba. Ann. Mus. Royal Congo Belge, Tervuren (Belgique), Série in-8. Sci. Geol. 29, 210 pp.

Cahen, L., Ferrand, J.J., Haarsma, M.J.F., Lepersonne, J., Verbeek, Th., 1960. Description du sondage de Dekese. Ann. Mus. Royal Congo Belge, Tervuren (Belgique), Série in-8. Sci. Geol. 34, 115 pp.

Celli, N.L., Lebedev, S., Schaeffer, A.J., Gaina, C., 2020. African cratonic lithosphere carved by mantle plumes. Nat. Commun. 11, 92. https://doi.org/10.1038/s41467-019-13871-2.

Cordell, L., Zorin, Y.A., Keller, G.R., 1991. The decompensative gravity anomaly and deep structure of the region of the Rio Grande rift. Journal of Geophysical Research: Solid Earth (1978–2012) 96 (B4), 6557–6568.

Collins, A.S., Pisarevsky, S.A., 2005. Amalgamating eastern Gondwana: The evolution of the Circum-Indian Orogens. Earth-Sciences Reviews 71, 229–270. https://doi.org/10.1016/j.earscirev.2005.02.004.

Crosby, A.G., Fishwick, S., White, N., 2010. Structure and evolution of the intracratonic Congo Basin. Geochemistry Geophysics Geosystems 11 (6), Q06010. https://doi.org/10.1029/2009GC003014.

Daly, M.C., Lawrence, S.R., Diemu-Tshiband, K., Matouana, B., 1992. Tectonic evolution of the Cuvette Centrale, Zaire. J. Geol. Soc. Lond. 149, 539–546. https://doi.org/10.1144/gsjgs.149.4.0539.

De Wit, M.J., Ransome, I.G.D., 1992. Inversion Tectonics of the Cape Fold Belt Regional inversion tectonics along the southern margin of Gondwana. In: De Wit, M.J., Ransome, I.G.D. (Eds.), Inversion Tectonics of the Cape Fold Belt Regional inversion tectonics along the southern margin of Gondwana. Karoo and Cretaceous Basins of Southern Africa. Balkema. Rotterdam 15–21.

De Waele, B., Johnson, S.P., Pisarevsky, S.A., 2008. Palaeoproterozoic to Neoproterozoic growth and evolution of the eastern Congo Craton: its role in the Rodinia puzzle. Precambrian Res. 160, 127–141.

De Wit, M.J., Linol, B., 2015. Precambrian basement of the Congo Basin and its flanking terrains. In: de Wit, M., Guillocheau, F., de Wit, M.C.J. (Eds.), The Geology and Resource Potential of the Congo Basin. Springer, Berlin, pp. 19–40. https://doi.org/10.1007/978-3-642-29482-2_2.

Delvaux, D., Maddaloni, F., Tesauro, M., Braitenberg, C., 2021. The Congo Basin: Stratigraphy and subsurface structure defined by regional seismic reflection, refraction and well data. Glob. Planet. Chang. 198, 103407. https://doi.org/10.1016/j.gloplacha.2020.103407.

Downey, N.J., Gurnis, M., 2009. Instantaneous dynamics of the cratonic Congo Basin. J. Geophys. Res. 114, B06401 https://doi.org/10.1029/2008JB006066.

Esso Zaire, SARL, 1981a. Geological Completion Report: Gilson-1 (Unpublished report).

Esso Zaire, SARL, 1981b. Geological Completion Report: Mbandaka-1 (Unpublished report).

Finger, N.P., Kaban, M.K., Tesauro, M., Mooney, W.D., Thomas, M.A., 2021. An integrated thermo-compositional model of the African cratonic lithosphere from gravity and seismic data. In: EGU21-15215. https://doi.org/10.5194/egusphere-egu21-15215 (EGU General Assembly 2021).

Förste, C., Bruinsma, S.L., Abrikosov, O., Lemoine, J.-M., Marty, J.C., Flechtner, F., Balmino, G., Barthelmes, F., Biancale, R., 2014. EIGEN-6C4 the latest combined global gravity field model including GOCE data up to degree and order 2190 of GFZ Potsdam and GRGS Toulouse. GFZ Data Services. https://doi.org/10.5880/ICGEM.2015.1.

Foster, D.A., Goscombe, B.D., Newstead, B., Mapani, B., Mueller, P.A., Gregory, L.C., Muvangua, E., 2015. U–Pb age and Lu–Hf isotopic data of detrital zircons from the Neoproterozoic Damara Sequence: Implications for Congo and Kalahari before Gondwana. Gondwana Res. 28 (1), 179–190. https://doi.org/10.1016/j.gr.2014.04.011.

Frimmel, H.E., Tack, L., Basei, M.S., Nutman, A.P., Boven, A., 2006. Provenance and chemostratigraphy of the Neoproterozoic West Congolian Group in Democratic Republic of Congo. Journal of African Earth Sciences 46, 221–239.

Fritz, H., Abdelsalam, M., Ali, K.A., Bingen, B., Collins, A.S., Fowler, A.R., Ghebreab, W., Hauzenberger, C.A., Johnson, P.R., Kusky, T.M., Macey, P., Muhongo, S., Stern, R.J., Viola, G., 2013. Orogen styles in the East African Orogen: a review of the Neoproterozoic to Cambrian tectonic evolution. J. Afr. Earth Sci. 86, 65–106.

Gray, D.R., Foster, D.A., Meert, J.G., Goscombe, B.D., Armstrong, R., Trouw, R.A.J., Passchier, C.W., 2008. A Damara orogen perspective on the assembly of southwestern Gondwana. Geol. Soc. Lond., Spec. Publ. 294, 257–278. https://doi.org/10.1144/SP294.14.

Grombein, T., Seitz, K., Heck, B., 2016. The Rock-Water-Ice topographic gravity field model RWI_TOPO_2015 and its comparison to a conventional rock-equivalent version. Surv. Geophys. 37 (5), 937–976. https://doi.org/10.1007/s10712-016-9376-0.

Haeger, C., Kaban, M.K., 2019. Decompensative gravity anomalies reveal the structure of the upper crust of Antarctica. Pure and Applied Geophysics 1–14. https://doi.org/10.1007/s00024-019-02212-5.

Hildenbrand, T.G., Griscom, A., Van Schmus, W.R., Stuart, W.D., 1996. Quantitative investigations of the Missouri gravity low: a possible expression of a large, Late Precambrian batholith intersecting the New Madrid seismic zone. Journal of Geophysical Research: Solid Earth 101 (B10), 21921–21942.

Hirt, C., Rexer, M., 2015. Earth2014: 1 arc-min shape, topography, bedrock and ice-sheet models – available as gridded data and degree-10,800 spherical harmonics. Int. J. Appl. Earth Obs. Geoinf. 39, 103–112. https://doi.org/10.1016/j.jag.2015.03.001.

JNOC, 1984. Rapport des investigations géophysiques et géologiques dans la Cuvette centrale de la République du Zaïre. Japan National Oil Corporation, Report for Department of Mines and Energy, Government of Zaire (Unpublished, 205 pp.).

Kaban, M.K., El Khrepy, S., Al-Arifi, N., 2017. Importance of the decompensative correction of the gravity field for study of the upper crust: application to the Arabian plate and surroundings. Pure Appl. Geophys. 174 (1), 349–358.

Kaban, M.K., Delvaux, D., Maddaloni, F., Tesauro, M., Braitenberg, C., Petrunin, A., El Khrepy, S., 2021. Thickness of sediments in the Congo Basin based on 1 the analysis of decompensative gravity anomalies. J. Afr. Earth Sci. 179, 104201. https://doi.org/10.1016/j.jafrearsci.2021.104201.

Kadima, E.K., 2011. Contribution géophysique à la connaissance du bassin de la Cuvette congolaise. In: Modélisation de la structure sédimentaire, Mécanisme de subsidence et structure de la lithosphère sous-jacente. University of Lubumbashi. PhD thesis. (278 pp.).

Kadima, E., Delvaux, D., Sebaganzi, S.M.N., Tack, L., Kabeya, S.M., 2011a. Structure and geological history of the Congo Basin: an integrated interpretation of gravity, magnetic, and reflection seismic data. Basin Res. 23, 499–527. https://doi.org/10.1111/j.1365-2117.2011.00500.x.

Kadima, E.K., Sebagenzi, S.M.N., Lucazeau, F., 2011b. A Proterozoic-rift origin for the structure and the evolution of the cratonic Congo Basin. Earth Planet. Sci. Lett. 304, 240–250.

Kadima, K.E., Delvaux, D., Everaerts, M., Sebagenzi, S.M.N., Lucazeau, F., 2015. Neoproterozoic to Early Paleozoic sequences of Congo Shield: comparison of Congo Basin with the surrounding marginal basins. In: de Wit, M., Guillochau, F., de Wit, M.C.J. (Eds.), The Geology and Resource Potential of the Congo Basin, Regional Geology Reviews. Springer, Heidelberg, pp. 97–109. https://doi.org/10.1007/978-3-642-29482-26.

Klein, George deV., Hsui, Albert T., 1987. Origin of cratonic basins. Geology 15 (12), 1094–1098 https://doi.org/10.1130/0091-7613(1987)15<1094:OOCB>2.0.CO;2.

Lawrence, S., Makazu, M.M., 1988. Zaire's Central basin: prospectivity outlook. Oil Gas Journal 86 (38), 105–108.

Lindsay, J.F., 2002. Supersequences, superbasins, supercontinents-evidence from the Neoproterozoic-Early Paleozoic basins of Central Australia. Basin Res. 14, 207–223.

Linol, B., de Wit, M.J., Barton, E., de Wit, M.C.J., Guillocheau, F., 2016. U–Pb detrital zircon dates and source provenance analysis of Phanerozoic sequences of the Congo Basin, central Gondwana. Gondwana Res. 29, 208–219.

Maddaloni, F., Pivetta, T., Braitenberg, C., 2021. Gravimetry and petrophysics for defining the intracratonic and rift basins of the western-central Africa zone. Geophysics (accepted). GEO-2019-0522.R4.

Martins, C.M., Barbosa, V.C.F., Silva, J.B.C., 2010. Simultaneous 3D depth-to-basement and density-contrast estimates using gravity data and depth control at few points. Geophysics 75 (3), XI21–I28. https://doi.org/10.1190/1.3380225.

Master, S., 2010. Lac Télé structure, Republic of Congo: Geological setting of a cryptozoological and biodiversity hotspot, and evidence against an impact origin. J. Afr. Earth Sci. 58, 667–679.

Ojo, A.O., Weisen, S., Ni, S., Zhao, L., Xie, J., Kao, H., 2020. Lithospheric Structure of Africa and Surrounding Regions Revealed by Earthquake and Ambient Noise Surface Wave Tomography. https://doi.org/10.1002/essoar.10504718.1.

Perron, P., Guiraud, M., Vennin, E., Moretti, I., Portier, É., Le Pourhiet, L., Konaté, M., 2018. Influence of basement heterogeneity on the architecture of low subsidence rate Paleozoic intracratonic basins (Reggane, Ahnet, Mouydir and Illizi basins, Hoggar Massif). Solid Earth 9 (6), 1239–1275. https://doi.org/10.5194/se-9-1239-2018.

Pivetta, T., Braitenberg, C., 2020. Sensitivity of gravity and topography regressions to earth and planetary structures. Tectonophysics 774, 228–299. https://doi.org/10.1016/j.tecto.2019.228299.

Raveloson, A., Nyblade, A., Durrheim, R., 2021. Joint inversion of surface wave and gravity data reveals subbasin architecture of the Congo Basin. Geology. https://doi.org/10.1130/G48408.1.

Rexer, M., Hirt, C., Claessens, S., Tenzer, R., 2016. Layer-Based Modelling of the Earth's Gravitational Potential up to 10-km Scale in Spherical Harmonics in Spherical and Ellipsoidal Approximation. Surv in Geophy, 37. https://doi.org/10.1007/s10712-016-9382-2.

Roberts, E.M., Jelsma, R.E., Hegna, T.A., 2015. Mesozoic sedimentary cover sequences of the Congo Basin in the Kasaï Region, Democratic Republic of Congo. In: de Wit, M., Guillocheau, F., de Wit, M.C.J. (Eds.), The Geology and Resource Potential of the Congo Basin. Springer, Berlin, pp. 163–191. https://doi.org/10.1007/978-3-642-29482-2_9.

Stolk, W., Kaban, M.K., Beekman, F., Tesauro, M., Mooney, W.D., Cloetingh, S., 2013. High-resolution regional crustal models from irregularly distributed data: application to Asia and adjacent areas. Tectonophysics 602, 55–68.

Tesauro, M., Kaban, M.K., Aitken, A.R.A., 2020. Thermal and compositional anomalies of the Australian upper mantle from seismic and gravity data. Geochem. Geophys. Geosyst. 21, 11. https://doi.org/10.1029/2020GC009305.

Turcotte, D.L., Schubert, G., 1982. Geodynamics, 2nd edn. Cambridge University Press, Cambridge, United Kingdom.

Uieda, L., Barbosa, V., Braitenberg, C., 2016. Tesseroids: forward-modeling gravitational fields in spherical coordinates. Geophysics F41–F48. https://doi.org/10.1190/geo2015-0204.1.

Watts, A.B., 2001. Isostasy and Flexure of the Lithosphere. Cambridge University Press, Cambridge; New York.

Watts, A.B., Tozer, B., Daly, M.C., Smith, J., 2018. A comparative study of the Parnaíba, Michigan and Congo cratonic basins. Geol. Soc. Lond., Spec. Publ. 472, 1–15. https://doi.org/10.1144/SP472.6.

Wilson, D., Aster, R., West, M., Ni, J., Grand, S., Gao, W., Patel, P., 2005. Lithospheric structure of the Rio Grande rift. Nature 433 (7028), 851–855.

Zorin, Y.A., Pismenny, B.M., Novoselova, M.R., Turutanov, E.K., 1985. Decompensative gravity anomalies. Geol. Geofiz. 8, 104–108.